	1.0		4.5 5.0 5.6 6.3 7.1 8.0	2.8	2.5
				3.2	2.2
				3.6	
	1.1			4.0	2.0
					1.8
1.25		1.4		1.6	

MICROCOPY RESOLUTION TEST CHART

NATIONAL BUREAU OF STANDARDS-1963-A

SECURITY CLASSIFICATION OF THIS PAGE *(When Data Entered)*

REPORT DOCUMENTATION PAGE	READ INSTRUCTIONS BEFORE COMPLETING FORM

1. REPORT NUMBER	2. GOVT ACCESSION NO.	3. RECIPIENT'S CATALOG NUMBER
AFOSR-TR- 83-0152	AD-A126812	

4. TITLE *(and Subtitle)*	5. TYPE OF REPORT & PERIOD COVERED
APPLICATION OF COMPUTERIZED TOMOGRAPHY FOR NONDESTRUCTIVE EVALUATION OF WELDMENTS	Final 82APR01- 82 Sept 30
	6. PERFORMING ORG. REPORT NUMBER

7. AUTHOR(s)	8. CONTRACT OR GRANT NUMBER(s)
Ira Lon Morgan Sulaksh Gautam	F49620-82-C-0068

9. PERFORMING ORGANIZATION NAME AND ADDRESS	10. PROGRAM ELEMENT, PROJECT, TASK AREA & WORK UNIT NUMBERS
Scientific Measurement Systems, Inc. 2808 Longhorn Blvd., Suite 303 Austin, Texas 78759	2305/K1 61102F

11. CONTROLLING OFFICE NAME AND ADDRESS	12. REPORT DATE
USAF, AFSC Air Force Office of Scientific Research /NE Bldg 410, Bolling AFB DC 20332	18 Feb 1983
	13. NUMBER OF PAGES
	86/w title page

14. MONITORING AGENCY NAME & ADDRESS(if different from Controlling Office)	15. SECURITY CLASS. *(of this report)*
	UNCLASSIFIED
	15a. DECLASSIFICATION/DOWNGRADING SCHEDULE

16. DISTRIBUTION STATEMENT *(of this Report)*

Approved for public release; distribution unlimited.

17. DISTRIBUTION STATEMENT *(of the abstract entered in Block 20, if different from Report)*

18. SUPPLEMENTARY NOTES

19. KEY WORDS *(Continue on reverse side if necessary and identify by block number)*

Computerized Tomography	Nondestructive Testing
Tomography	Electron Beam Weld Testing
Gamma Ray Scanning	Three Dimensional Imaging
Weldment Testing	Inspection in Automated Manufacturing

20. ABSTRACT *(Continue on reverse side if necessary and identify by block number)*

The purpose of this research project has been to investigate the feasibility of applying the Computerized Tomographic (CT) processes to the nondestructive testing and evaluation of weldments. The present study investigates the degree of spatial resolution obtainable via tomographic techniques as a function of the tomographic parameters. The scope of work has included a study of the applicability of CT processes for on-line quasi real time

DD $^{FORM}_{1\ JAN\ 73}$ 1473 EDITION OF 1 NOV 65 IS OBSOLETE

SECURITY CLASSIFICATION OF THIS PAGE *(When Data Entered)*

Block 20 continued:

inspection of automated welding processes.

The feasibility study included CT examinations of electron beam weldments on rocket motor casings, weldments on a cast aluminum object, and several plate weldments. The main objective was to study the influence of the tomographic parameters on the resolution of the weldment features. A technique for rapid on-line, quasi real time inspection of weldments on a rocket motor casing is demonstrated. Tomographic evaluations were compared with available radiographic evaluations to study the relative merits of these techniques.

The results of the present study have indicated the potential feasibility of applying CT techniques to the general area of weldments, including on-line inspection of automated welding processes. The results also indicate the need for further research and provide guidelines for improving spatial resolution.

In addition to their applications for nondestructive inspection and evaluation of weldments, CT techniques have potential applicability to a wide range of industrial as well as academic pursuits.

Accession For

NTIS CRA&I ✓
DTIC TAB ☐
Unannounced ☐
Justification

By
Distribution/
Availability Codes

Dist	Avail and/or Special

Final Report

on the

Application of Computerized Tomography

for Nondestructive Evaluation of Weldments

Submitted to

Air Force Office of Scientific Research
Bolling AFB, DC

Contract #F49620-82-C-0068

Submitted by

Scientific Measurement Systems, Inc.
2808 Longhorn Blvd., Suite 303
Austin, Texas   78759

February 18, 1983

TABLE OF CONTENTS

1. INTRODUCTION

A wide range of industrial activities are in need of techniques to implement rapid and efficient nondestructive testing (NDT), and non-destructive evaluation (NDE). Computerized Tomography (CT) is an innovative technique involving three-dimensional imaging methods (1).

CT techniques have been successfully employed in the field of medical diagnostics for over a decade. Although CT has undergone significant development in the medical field, its application to industrial situations has received little attention. Only recently have the advantages of tomography for industrial NDE become apparent.

The process of Computerized Tomography involves acquisition of information on the interior of an object, without intruding into the object. It is based on the physical principles underlying the inter-action of electromagnetic radiation with matter. The measurement of photon transmission through an object yields an image of the object cross-section examined. The image obtained is called a tomogram.

The data contained in a tomogram are in a digital matrix form, and easily afford rapid and quantitative analysis via computer algorithms. Conventional film radiographic techniques, on the other hand, often require a long time for completion and suffer from inevitable subjective evaluation. As in the case of real-time fluoroscopy, radiographic methods suffer contrast degradation, leading to difficulties in their subjective interpretations.

The primary aim of the present research was to investigate the feasibility of applying CT techniques to the nondestructive testing of

various types of weldments. The emphasis was placed on detecting typical defects such as lack of fusion, porosity, and misjoints. The weldments which were investigated were electron beam (EB) welds on rocket motor casings, welds in cast aluminum objects, and some plate weldments. The scope of work included a study of the applicability of the CT techniques for on-line inspection of automated welding processes.

A laboratory experiment was performed to simulate an automated welding process and an on-line CT inspection. The weldment used for this study, as well as the EB welds, were designed to include typical weld defects.

The spatial resolution obtainable from a CT examination of an object depends upon a number of tomographic parameters. These are the number of angular views, ray spacings in a fan beam, source-detector collimations, and exposure times. The research performed included a study of the spatial resolution as a function of these parameters. In addition, the effects of limit and angular view examinations on those situations where a 360 deg access to the object is not possible were included. The report is organized as follows:

In Section 2 a brief examination of the theoretical background is given. The laboratory high-energy tomograph used for the study is described in Section 3. The description of the various weld samples, the analysis of the tomograms obtained from CT examinations, and the results of the various studies are given in Section 4. Section 5 summarizes and concludes the present study, along with a discussion of the application of CT techniques as an on-line inspection method in automated welding processes.

2. Theoretical Background

Tomography is based on the phenomena of interaction between electro-magnetic radiation and matter. When a beam of gamma rays is transmitted through an object, it is known that the transmitted intensity, (I), is related to the incident intensity, (I_o), through the relation

$$I = I_o e^{-\mu \cdot x} \tag{1}$$

where μ is the linear attenuation coefficient characteristic of the medium, and x is the thickness of the material. Equation (1) implicitly assumes that the radiation is monochromatic and the medium is homogeneous.

There are several physical processes through which the photon beam may be attenuated. There are three principal interactions, however, which are significant over different ranges of photon energies: (1) photoelectric capture (0.01 MeV – 0.5 MeV), (2) Compton Scattering (> 0.05 MeV), and (3) pair production (1.02 MeV and above). For the energies under consideration (< 1.3 MeV), photoelectric and Compton processes are dominant, and the contribution of pair production process to the beam attenuation is less than 1%. The linear attenuation coefficient, μ, in Equation (1), is the combination of attenuation obtained through these three processes. As the physical principles underlying these processes are well discussed in literature (2,3) we omit a discussion of these. We may summarize these processes by the relation,

$$\mu_{TOT} = \frac{\rho N_A}{A} \left[\mu_{PE} + \mu_C + \mu_{PP} \right] \tag{2}$$

3

where μ_{PE}, μ_C and μ_{PP} are the atomic attenuation coefficients due to photoelectric, Compton, and pair production processes respectively, and are given approximately by relations:

$$\mu_{PE} \sim K_{PE} \cdot Z^{4.5}/E^3$$

$$\mu_C \sim K_C \cdot f(E) \cdot Z$$

$$\mu_{PP} \sim K_{PP} \cdot Z^2 \cdot g(E) \tag{3}$$

where K's are constants, and $f(E)$ and $g(E)$ are photon energy dependent factors, ρ is the density; N_A, Avagadro's number; Z, the atomic number, and A, the atomic weight.

We may note in passing that the Compton process is ideally suited for measuring electron density distribution since it is directly proportional to Z.

The transmission relation, Equation (1), in view of Equation (3), is a function of photon energies. In the case of a nonhomogeneous medium, the transmitted intensity depends also upon the distribution of mass along any given ray path. In view of these considerations, Equation (1) generalizes to,

$$I(x,E) = I_o(x_o,E) \; e^{-\int_{x_o}^{x} \mu(t,E)dt} \tag{4}$$

where t is the coordinate measured in the direction of the incident radiation and μ is the linear attenuation coefficient. The total absorption at a given energy of incident photons, along a line from x_o to x, is given

4

by

$$\int_{x_o}^{x} \mu(t,E)\,dt = \ln \frac{I_o(x_o,E)}{I(x,E)} \tag{5}$$

Notice that μ, the linear attenuation coefficient, is a function of the material properties of the object under examination. It contains information on the material properties of the object, if the photon energy is known. Ignoring the pair production effect, the function $\mu(x,E)$ may be approximated using Equation 2, i.e.,

$$\mu(x,E) \stackrel{\sim}{=} \left\{ \frac{\rho(x)Z(x)N_A}{A(x)} \right\} \left(K_{PE} Z^{3.5}(x)/_E{}^3 + K_C f(E) \right) \tag{6}$$

The first factor in parentheses represents the electron density at a position x along the ray. Rewriting Equation (5), we have

$$\int_{x_o}^{x} e_d(t) \cdot \left[K_{PE} \cdot Z^{3.5}(t)/_E{}^3 + K_C f(E) \right] dt = \ln \frac{I_o(x_o,E)}{I(x,E)} \tag{7}$$

where $e_d(x)$ is the electron density.

Equation (7) may be generalized to two dimensions to mathematically analyze the tomographic "reconstruction" process. The following equation describes the attenuation along a scan line in any section ("tomos") of an object, (see Fig. 1).

Figure 1

6
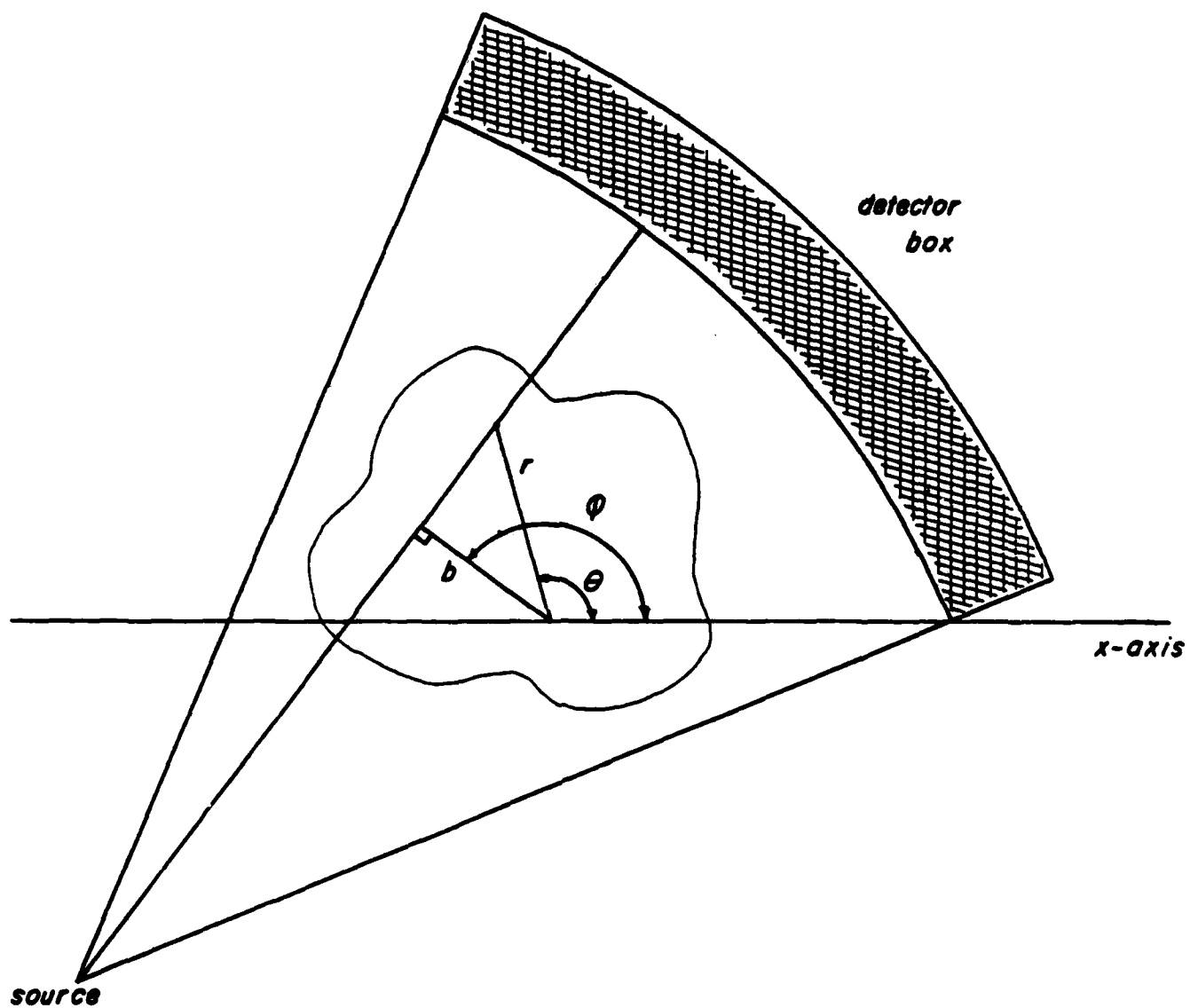
$$\mathcal{L}(b,\phi,E) = \int dr \int d\Theta \, e_d(r,\Theta) \cdot r \cdot \delta(b - r\cos(\Theta-\phi)) \cdot$$

$$\left[K_{PE} Z^{3.5}(r,\Theta)/E^3 + K_C F(E) \right]$$

where,

$$\mathcal{L}(b,\phi,E) = \ln I_o(b,\phi,E)/I(b,\phi,E) \tag{8}$$

ϕ is the inclination of the scan line with the x-axis (polar axis) and b is the perpendicular distance from the origin to the line. Inversion of Equation (8) is the essential basis for reconstruction of the object plane in which the transmission data are collected. In the absence of the photoelectric effect, inversion of Equation (8) produces the electron density map of a given object plane, which is closely related to the mass density distribution of the object.

Equation (8) represents a relationship for an ideal case consisting of point sources and point detectors. In practice, both the source as well as the detectors have finite apertures, and the transmission data is obtained over a strip of finite area rather than along a ray. The source-detector geometry, thus, defines the sampling extent and, consequently, the spatial resolution.

In most systems requiring nondestructive testing and evaluation, an important criterion for assessing the applicability of a technique is the accuracy of the information obtained. In tomography, the quantity and the quality of the information depends on the number of scan views, the number of rays in a given beam (i.e. the number of detectors), the isotopic photon source characteristics, collimation of the source and detectors, and the exposure times.

7

3. Tomographic Setup

The SMS EM-1 laboratory tomographic scanner has been in successful operation for over four years. It is configured in a fan beam geometry with a source to detector distance of 122 cm, as shown in Fig. 2. The detector system consists of 31 individual NE102 scintillation detectors coupled to phototubes, all housed in a light-tight aluminum box. Photo-tube output is processed in the pulse (photon) counting mode with amplifier-discriminators and recorded digitally in scalers. Cross-sectional dimensions of the detectors are 6.4 mm (width) and 20.0 mm (height), with lengths varying from 125 mm to 250 mm, aligned radially from the source. The beam flux can be collimated at each detector by a continuously variable slot collimator, designed and fabricated at SMS. This variable collimator permits aperture widths from 0.0 to 5.5 mm and heights from 0.0 to 20 mm at each detector.

The photon source used in scanning is a 200 Ci Iridium-192 source housed in a standard radiographic device. Without the collimator, the beam flux produces a count-rate of $\sim$ 20 megahertz in the detectors, with no object intercepting the flux. The background count-rate, with appro-priate phototube voltages and thresholds, averages a few hundred hertz. Source collimation restricts the primary flux to a solid angle which falls within that defined by a highly absorptive front face of the lead colli-mator assembly. In this configuration the scattering is minimized. The height of the fan beam at the center of the source-detector separation is 5.0 mm with the present source collimator.

The object table is normally positioned halfway between the source and the detector, with a provision for locating it either closer to the

8
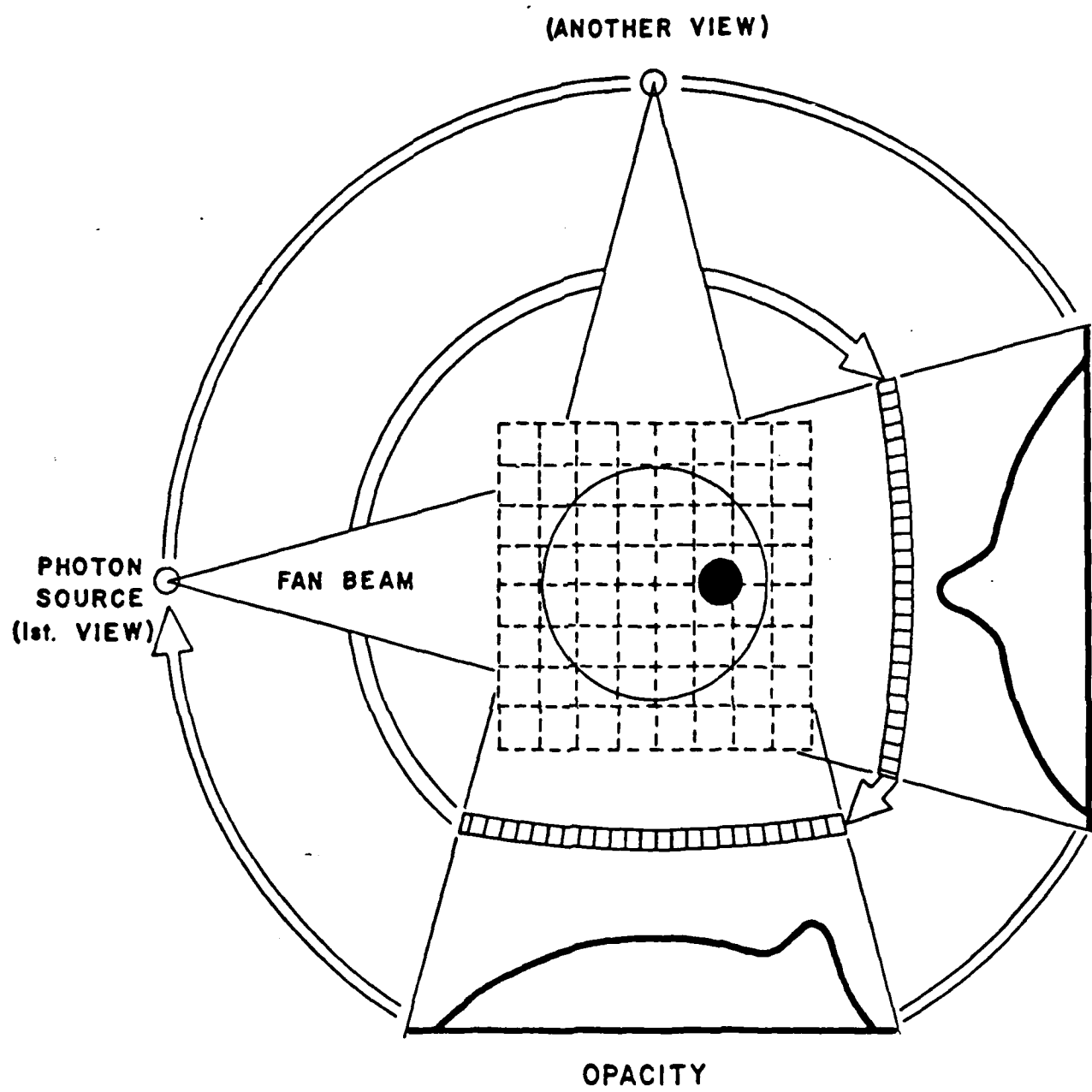
Figure 2. Fan beam geometry, including rotational motion characteristic of third generation scanners. The two dimensional matrix depicts the grid of pixels (elements of area) used for the reconstruction.

TOMOGRAPHIC SCANNING SYSTEM
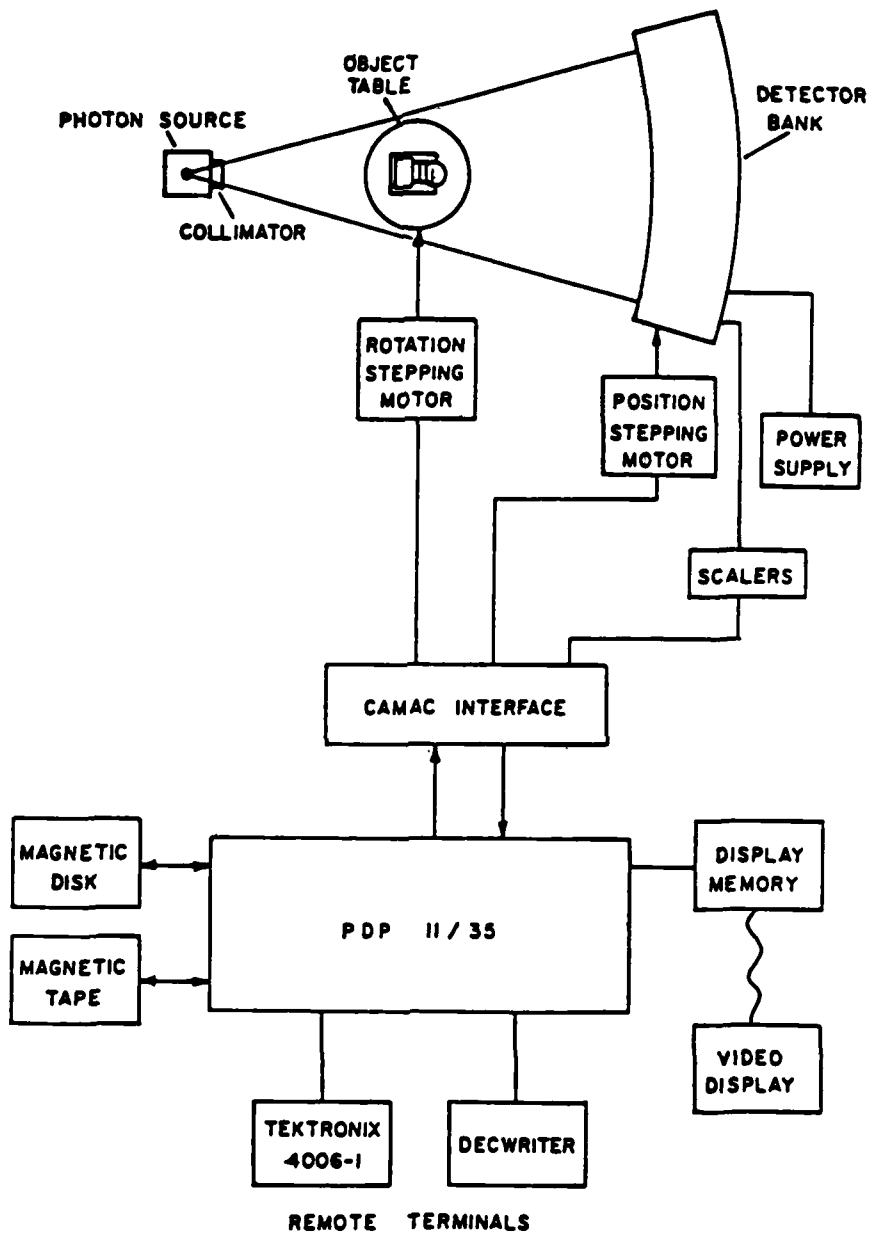
Figure 3

source or to the detector. The current SMS EM-1 scanner operates as a modified "third-generation" rotate-only tomograph. Given a fixed orientation of source and detector bank, the object table can be rotated through 360 deg, with data accumulation occurring at specified, regularly spaced angles within that range. These positions are termed as "views". The detector bank is then stepped sequentially to other positions within the angle defined by the axes of consecutive detectors, and the object rotation procedure is repeated at each of these detector bank positions. In this manner, the number of ray paths defined within the fan beam can be increased to any desired number.

As is evident from Fig. 3, the entire data taking process, with the exception of vertical positioning of the object (i.e., selection of a particular cross section at plane of the object), is accomplished automatically under control by a data acquisition program residing in the SMS-PDP 11/35. Positioning of the detector box, rotation of the object table, and periodic interrogation of the scalers recording the detection signals are performed in the above manner. Calibrations, including alignment of the detector bank to ensure proper geometry and recording detector counts with no object in place (i.e., "air count"), for normalizing transmission counts, are completed prior to data accumulation. For a major portion of the present study, data were taken for ten equally spaced positions of the detector box over the interval of 1.38 cm. Consequently adjacent rays in the fan beam subtended an angle of 0.0648 deg, producing a ray spacing at the center of rotation of the object of 0.69 mm. At each detector position data were obtained about 360 deg at regular angular increments of 0.9 deg providing a total of 400 angular positions and effectively producing 124,000 individual ray measurements.

11

4. Tomographic Examination

4.1 Description of the Samples and Scanning Parameters

Several weldment samples were procured from private and government agencies involved in Air Force and Aerospace related efforts. These samples are described below.

Two stainless steel rocket motor casings, 12.5 cm (5 in), and 20.0 cm (8 in) in diameter, respectively, containing weldments, were obtained from Hercules, Inc., MacGregor, Texas. Each casing contained three specially designed electron beam (EB) weldments. The weldments included typical weld defects such as lack of fusion, misjoints, porosity and cracks. The radiographic evaluations of these weldments are given in Table I. Such casings are used in the manufacture of rocket motors, and usually contain up to three welds per casing. At Hercules, Inc., the standard method for inspection is x-ray film radiography. The EB weldment samples were received along with radiographs of the welds for the purpose of comparison. A photograph of these samples is shown in Fig. 4.

TABLE I

EB Weldment Characteristics

| Weld Label	Five-inch Casing 0.065-inch wall thickness	Eight-inch Casing 0.105-inch wall thickness
A	Good	Good Overall Contains drop-through and undercut regions.
B	Lack of fusion	1. Rewelded once 2. Lack of fusion
C	1. One pore area 2. Two areas containing lack of fusion or missed joints	1. Lack of fusion 2. Porosity

12
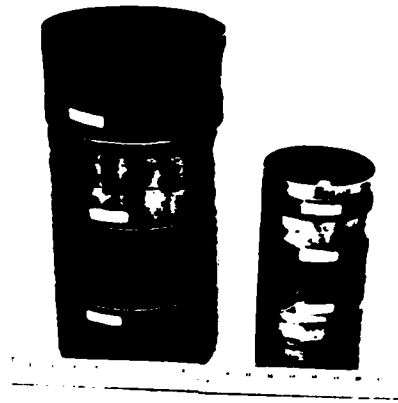
Fig. 4. Photograph of the eight-inch diameter and five-inch
diameter steel rocket motor casings obtained from Hercules,
Inc. Each casing has three EB welds, with the middle weld
without defects.
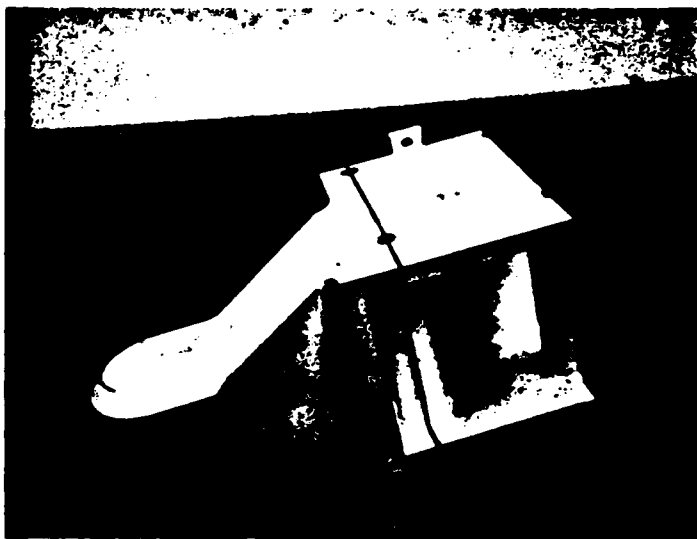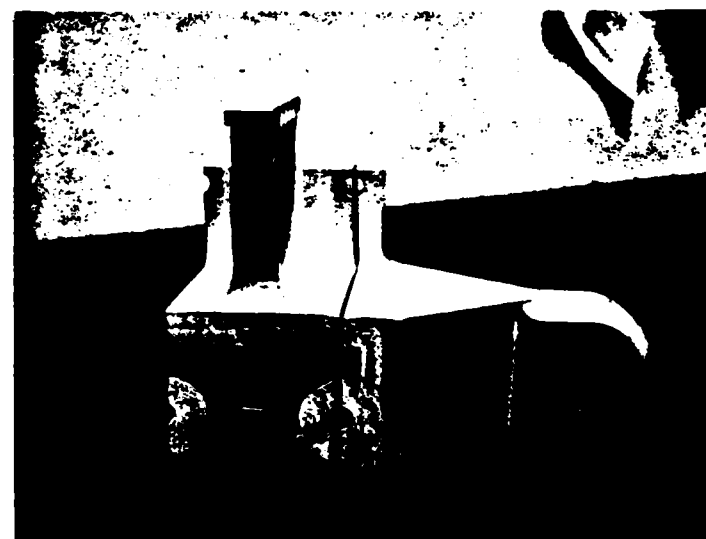
(a)   (b)

Fig. 5a and 5b. Two views of the cast aluminum component
obtained from The United Space Boosters, Ltd. The dark
line on the object surface marks the plane (slice) of CT
scan.

13

A cast aluminum component containing standard heliarc weldments was obtained from United Space Boosters, Ltd., Huntsville, Alabama. The component is a part of the Thrust Vector Control (TVC) mechanism of the Space Shuttle booster assembly. It contains an aluminum cylinder welded at both ends to an aluminum bracket. The object is shown in Figs. 5a and 5b, and the dark line on the object surface marks the cross-sectional plane examined. This particular sample was evaluated to be defective by the manufacturer via visual and dye penetrant methods. The defects contained in the sample were lack of fusion and cracks (voids) in the weldment.

A set of three thin plate weldments was obtained from the U. S. Air Force Kelly Supply Depot, San Antonio, Texas. These contained defects such as porosity and inclusions. The plates were representative of aircraft body and wing panels. These were accompanied by film radiographs. A photograph of these plates is shown in Fig. 6.

The samples described above were comprehensively scanned with 400 angular views, a ray spacing of 0.065 deg and a collimation of 1.5 mm (width) x 2.0 mm (height) at each detector. A 200 Ci Iridium-192 isotopic gamma ray source was used for the entire series of tomographic scans.

Several sets of tomograms were reconstructed from the comprehensive data. The first set of tomograms corresponded to a reconstruction of the entire cross section for each sample. In addition, tomograms of the regions of interest of the images were reconstructed using the entire set of data. These tomograms are referred to as Region of Interest Reconstruction (ROIR) tomograms. To study the parametric dependence of the spatial resolution, a set of tomograms corresponding to various
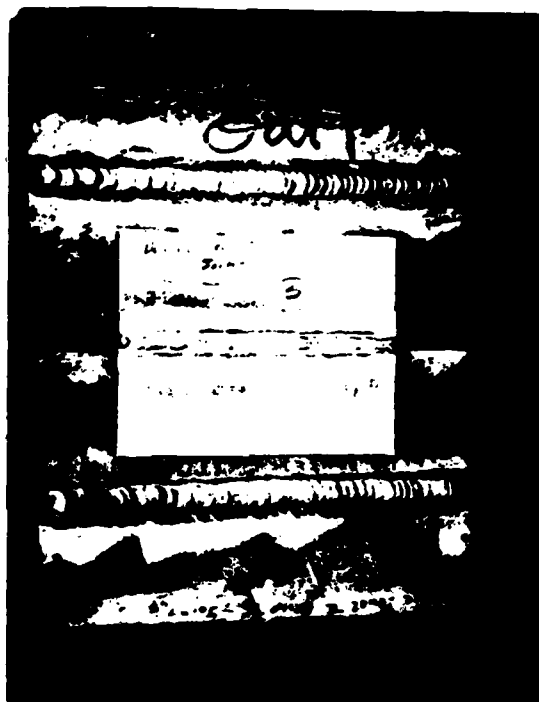
Fig. 6. Photograph of the three plate weldment samples
obtained from the U. S. Air Force Kelly Supply
Depot.

combinations of the angular views and ray spacings was reconstructed and analyzed. Two tomograms of the aluminum casting were reconstructed using limited data to study the extent of information obtained in partial view tomography.

These tomograms are analyzed below. A comparison with corresponding radiographs is given, wherever radiographs have been available.

4.2 Five-inch Rocket Motor Casing

We begin with the examination of weldments on the five-inch casing. The tomogram shown in Fig. 7 is the cross-sectional image of Weld #A. The reconstruction was made on a 256 x 256 grid with pixel dimensions of .63 mm x .63 mm. A metallic pin and a hollow cylinder were attached to the casings to provide a reference mark of the desired slice plane through the weld. Within the resolution afforded in the tomogram shown in Fig. 7, the weldment thickness is fairly uniform around the entire weldment. To study the weldment structure more closely, ROIR's of the four quadrants of the weldment were made on 256 x 256 grids with a finer pixel dimension of 0.3 mm x 0.3 mm. The corresponding tomograms are shown in Figures 8a to 8d. The good quality of this weldment is demonstrated by the uniformity of the weld thickness in each of the ROIR's The corresponding radiograph, shown in Fig. 9, is in agreement with the tomographic results. We note at this point that there is a basic difference between a CT image and a radiographic image. A radiographic image is a two-dimensional projection of the mass contained in the object, whereas, a CT image gives the mass distribution in the object cross section. A radiographic inspection does not provide any information on the location of a defect within the object in the direction along which the radiograph is

16
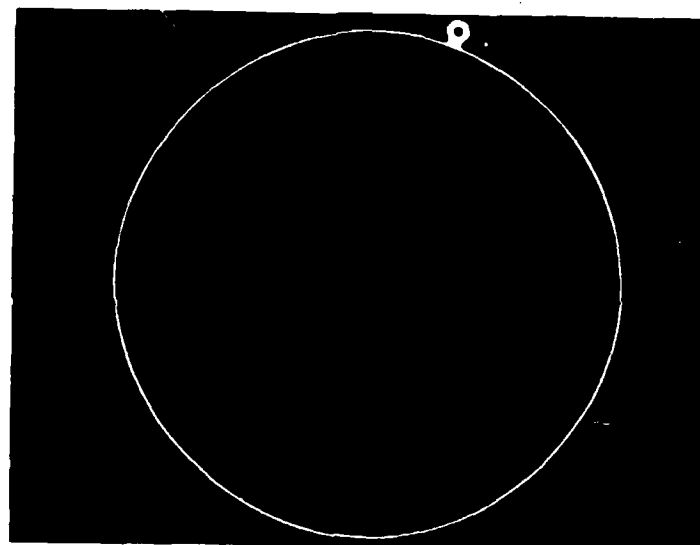
Fig. 7. Cross-sectional tomogram of the five-inch casing, weldment #A. Source: Ir-192. Grid: 256 x 256. Pixel dimensions: 0.63 mm x 0.63 mm.
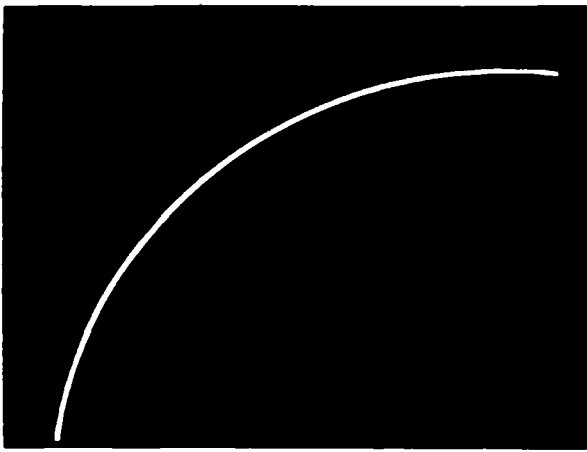
(a)
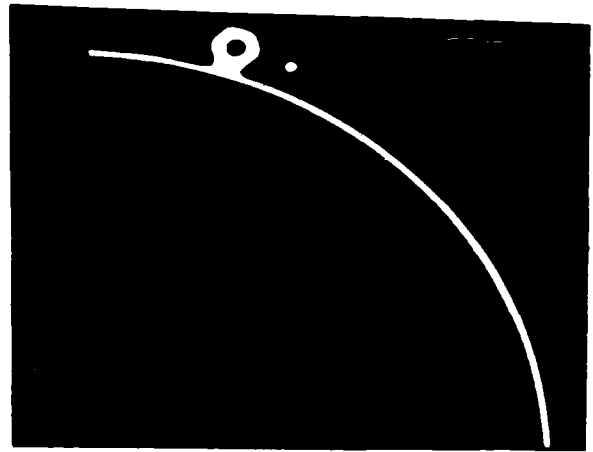
(b)
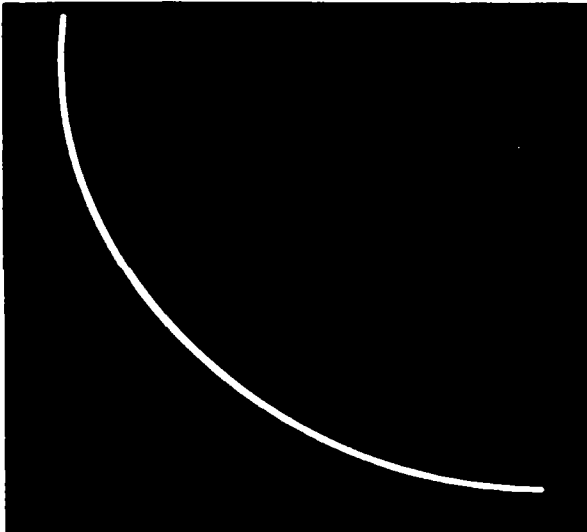
(c)
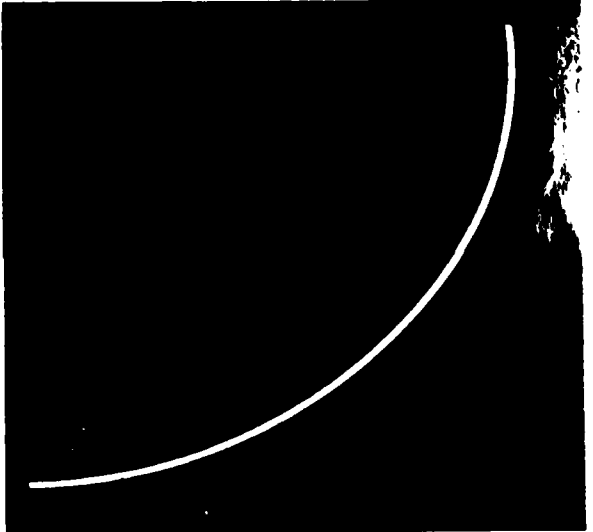
(d)

Fig. 8a-8b. Four quadrant ROIR of the tomogram of Fig. 7. The uniformity of the cross-sectional thickness is indicative of the good quality of the weldment.

18
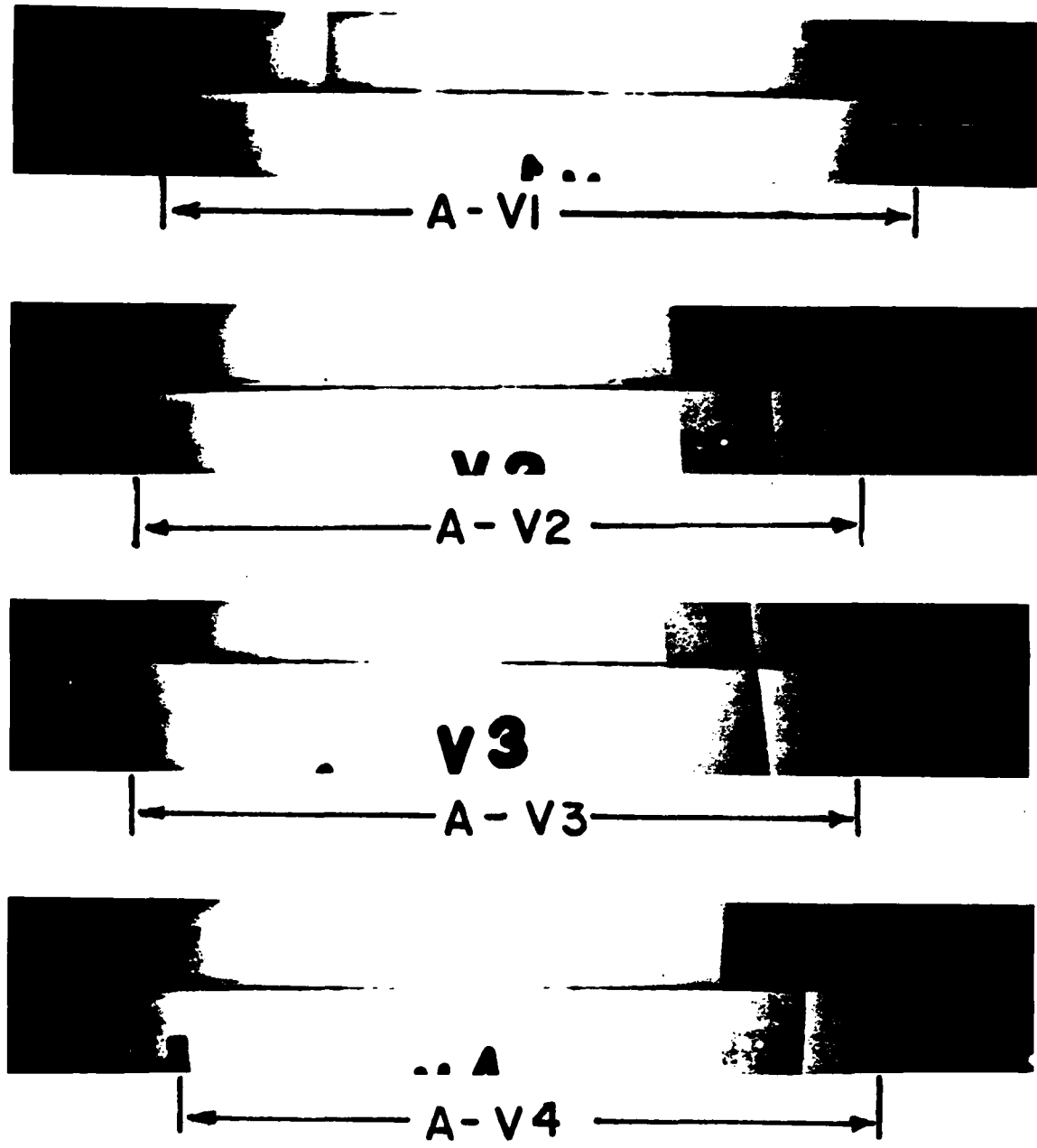
Fig. 9. Radiographic sections of the five-inch casing
weldment #A.

19

taken. With CT techniques, it is possible to accurately locate the region of defects, as well as measure their spatial extents. Later in this section we provide a demonstration of quantitative measurements afforded by CT methods.

The second set of tomograms corresponding to Weldment #B is shown in Figures 10 and 11a through 11d. Fig. 10 displays the total cross-sectional tomogram and the ROIR tomograms of the quadrants are displayed in Figs. 11a to 11d.. This weldment was designed to contain areas of lack of fusion and a region of missed joint caused by a deflection of the electron beam away from the weld seam. In Fig. 10 the region marked by points A_1 and B_I corresponds to a missed joint, i.e., an unwelded region. The other regions of missed joints are marked by (A_2, B_2) and (A_3, B_3). These regions are clearly detected in the radiographs shown in Fig. 12. They are also distinguishable in the tomogram of Fig. 10 and in the tomograms of the quadrants #1, #3 and #4, as extremely uniform wall thicknesses. If the casing were scanned prior to and after EB welding to provide information on changes in the boundary, the persistence of the wall uniformity would indicate missed joints.

This method relies on the fact that in EB welding the joint is sealed together only through heating, without any use of a soldering material. The mass in the weldment cross section, therefore, remains conserved and the effect of welding is to merely redistribute the mass. Such a redistribution of mass, manifest in the typical crown formation along EB welds, changes the shape of the cross section in relation to that of an unwelded joint. Even in the previous case, where a very good quality EB weldment was examined, a closer look reveals a variation in

20
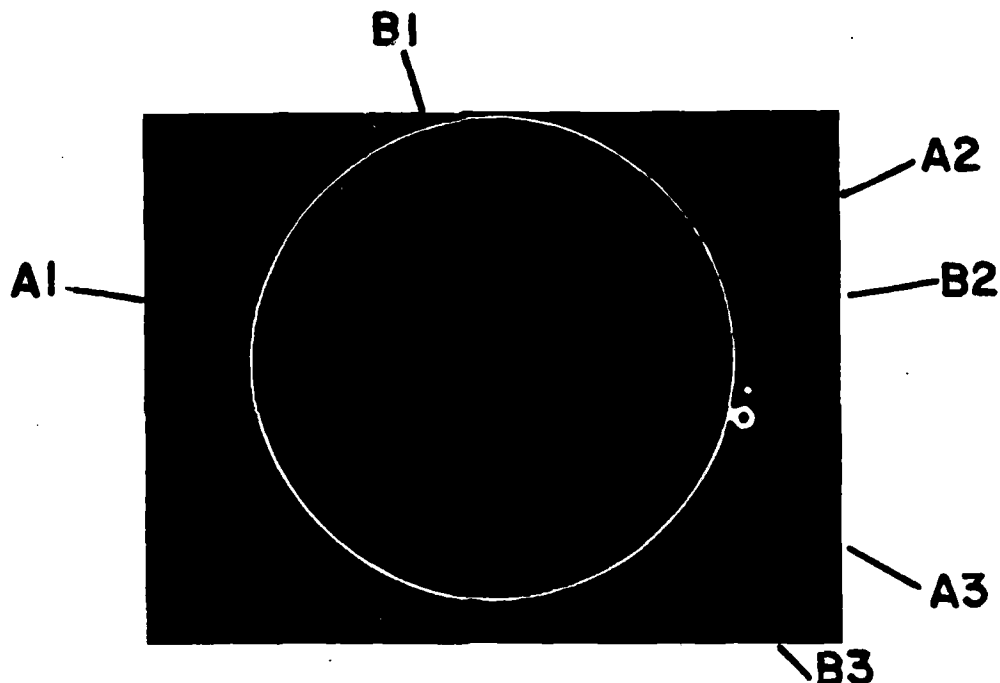
Fig. 10. Cross-sectional tomogram of the five-inch casing weldment #B. This weldment contains missed joints, the regions marked by (A_1, B_1), (A_2, B_2) and (A_3, B_3). Presence of missed joints is indicated by the uniformity of the cross-sectional thickness in these regions. Source: Ir-192. Grid: 256 x 256. Pixel dimensions: 0.63 mm x 0.63 mm.
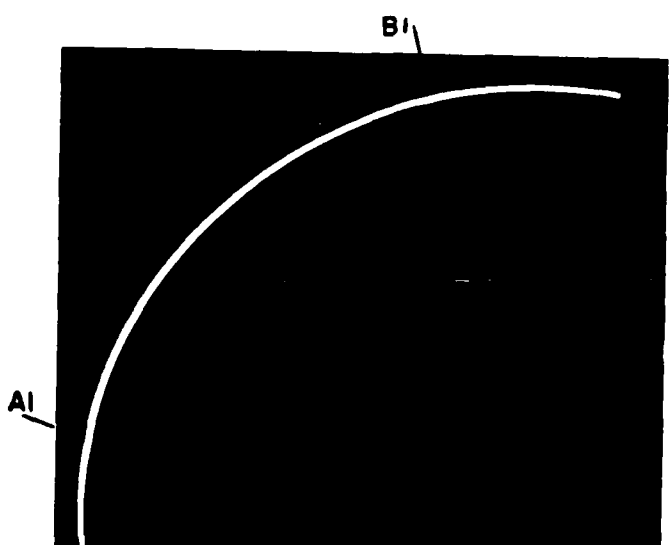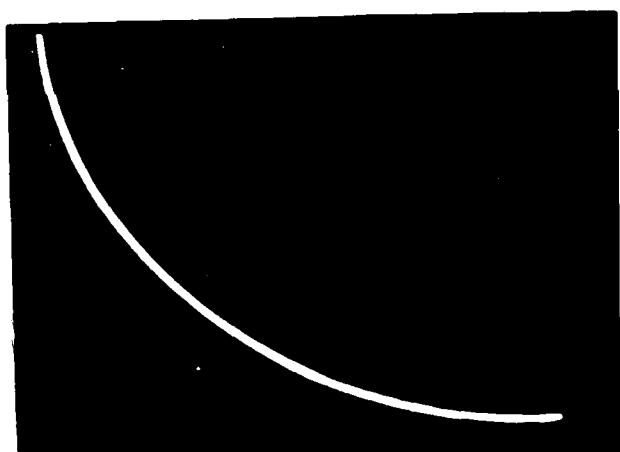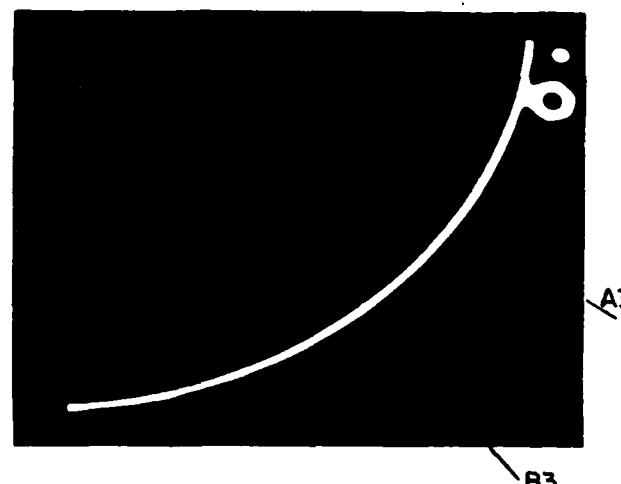
Fig. 11a-11d. Four quadrant RIOR of the tomogram of Fig. 10.
The regions of missed joints are marked by (A_1,B_1),
(A_2,B_2) and (A_3,B_3). Grid: 256 x 256.

Pixel dimensions: 0.3 mm x 0.3 mm.
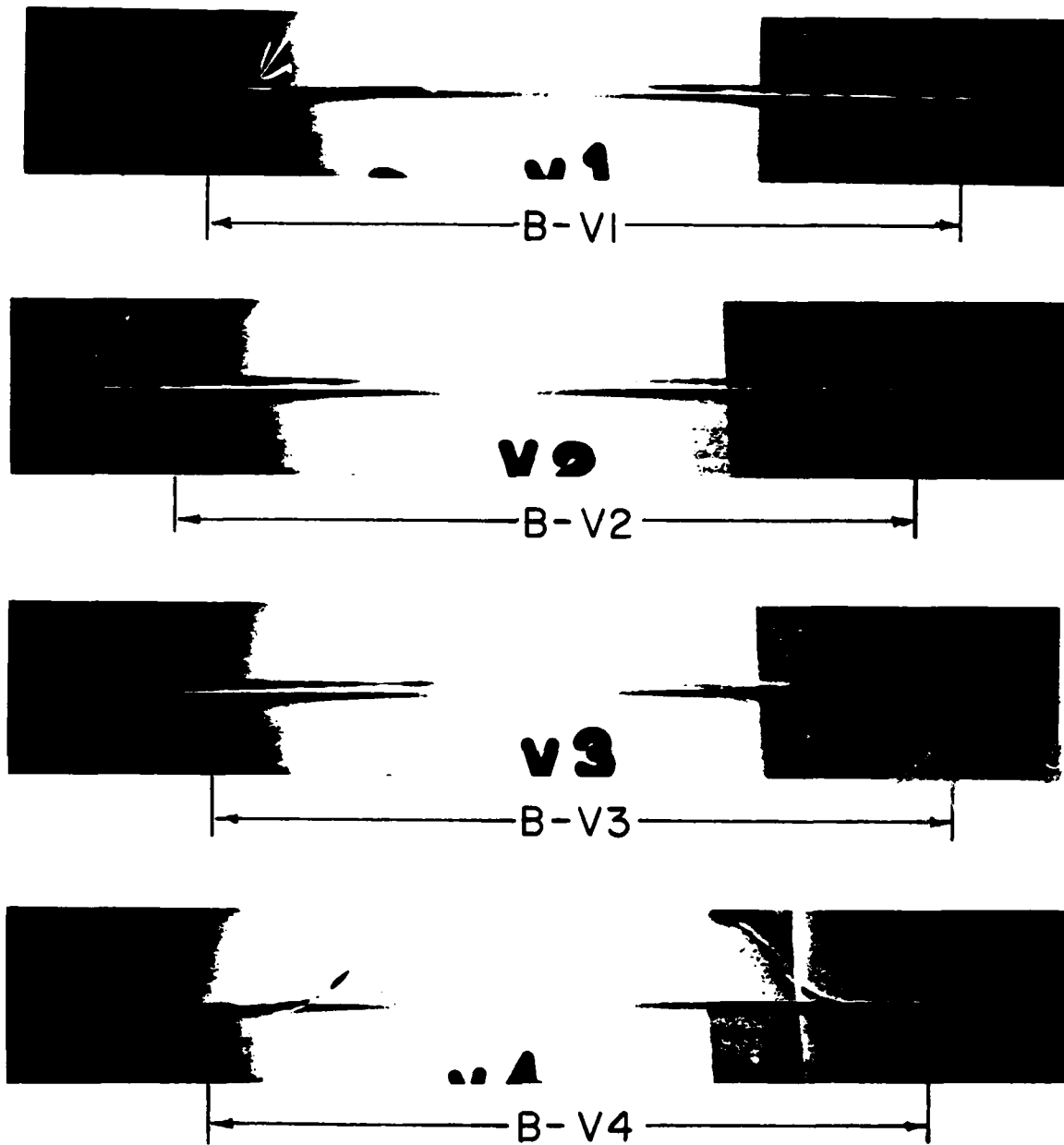
Fig. 12. Radiographic sections of the five-inch casing weldment #B. The region of weldment from the middle to the strip B-V1 to the middle of B-V2 contains lack of fusion and cracks. Strip B-V4 displays the missed joint caused by jogging of the electron beam.

23

the weldment cross section. We emphasize, however, that a mere visual determination of the weldment uniformity does not suffice to identify unambiguously missed joints. None the less, if the tomographic examination is conducted prior to and after the welding passes, accurate identification of defects is possible. We shall return to the discussion of such a method at a later point.

The region displayed in the tomogram shown in Fig. 11c is almost entirely a region of lack of fusion and cracks. The corresponding region on the radiograph ranges from the middle of the strip B-V1 up to the middle of B-V2 (See Fig. 12). The inability to observe clearly these regions in tomograms is due to the degree of collimations at the source and the detectors. The vertical extent of collimation apertures determines the thickness of the cross-sectional slice being examined. The difference in the mass densities over the slice thickness, i.e., in the vertical direction, is unresolved to an extent due to the averaging. In the setup used, the effective thickness of the slice, at the object cross section, was approximately 1.2 mm, and hence cracks of submillimeter dimensions remained unresolved. The resolution in the cross-sectional plane was better because the effective sampling extent in that plane was approximately 0.8 mm. This case serves as an example of how source-detector collimations can influence the degree of spatial resolution.

The next set of tomograms corresponds to Weld #C. The total cross-sectional tomogram is shown in Fig. 13, and the quadrant ROIR tomograms are shown in Figs. 14a to 14d. The weldment contains two areas of lack of fusion or missed joints, at locations marked A in Fig. 14b, and

24
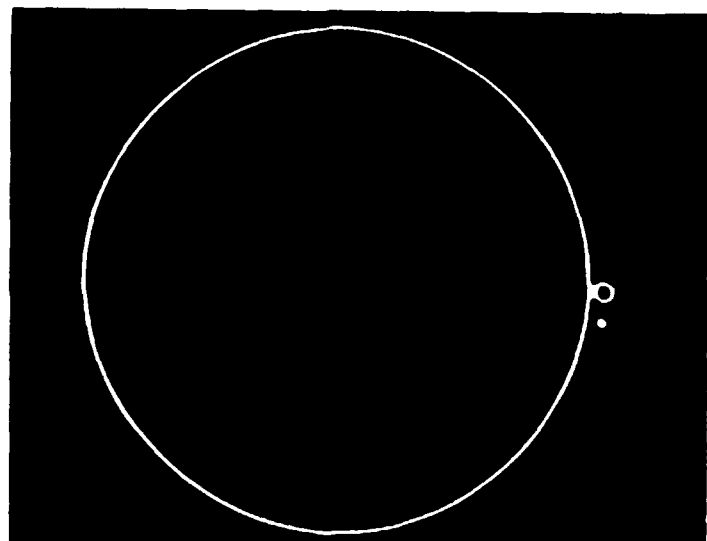
Fig. 13. Cross-sectional tomogram of the five-inch casing
weldment #C. Source: Ir-192. Grid: 256 x 256.
Pixel dimension: 0.63 mm x 0.63 mm.
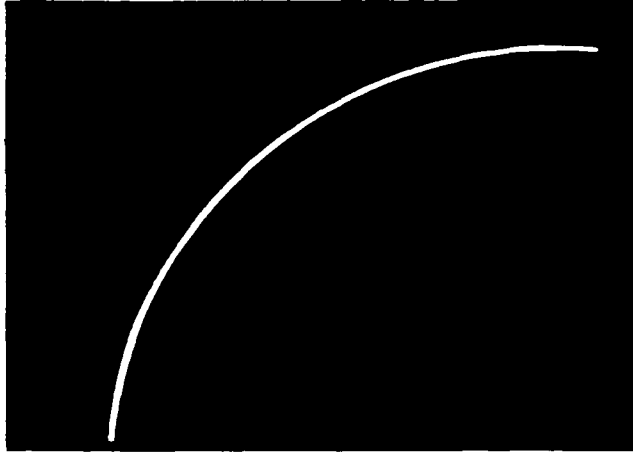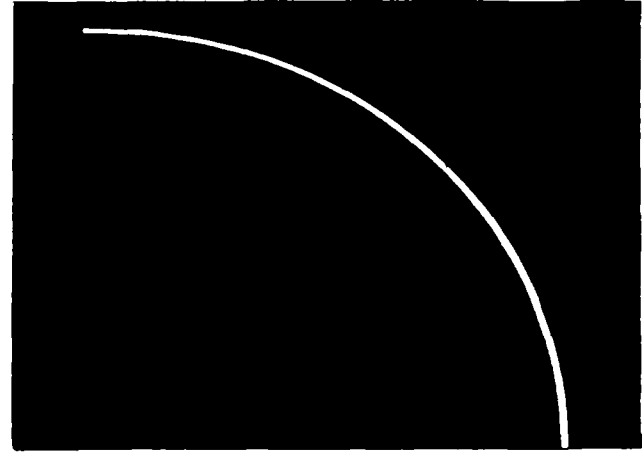
(a)   (b)

Fig. 14a-14d. Four quadrant RIOR of the tomogram of Fig. 13.
        Two areas of lack of fusion or missed joints are marked
        by A in 14b, and by B in 14d, indicated by the uniform
        thickness of the cross section in these regions.

26

(c)

(d)

27
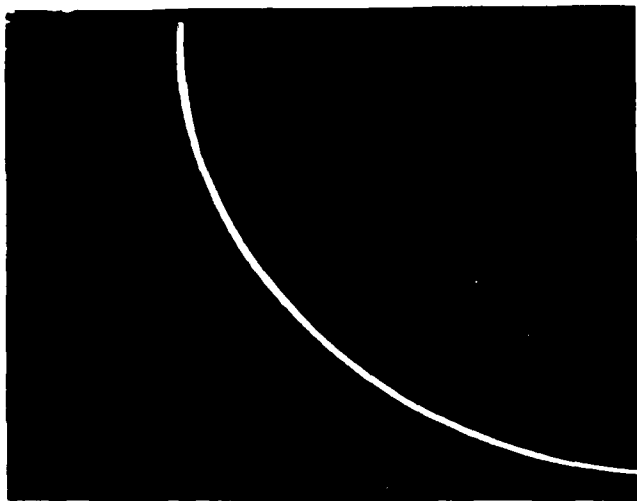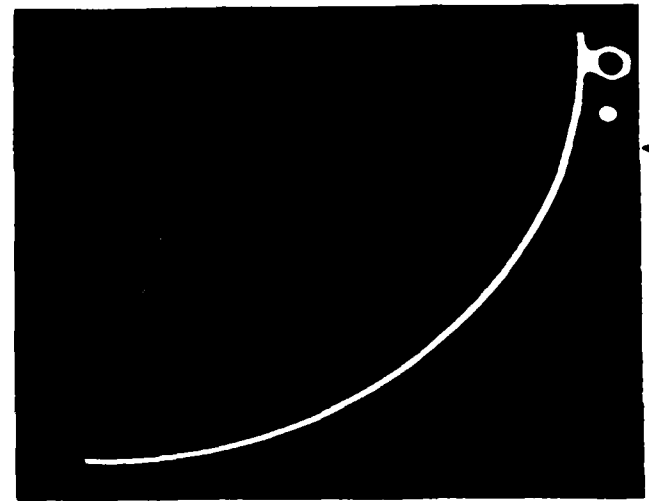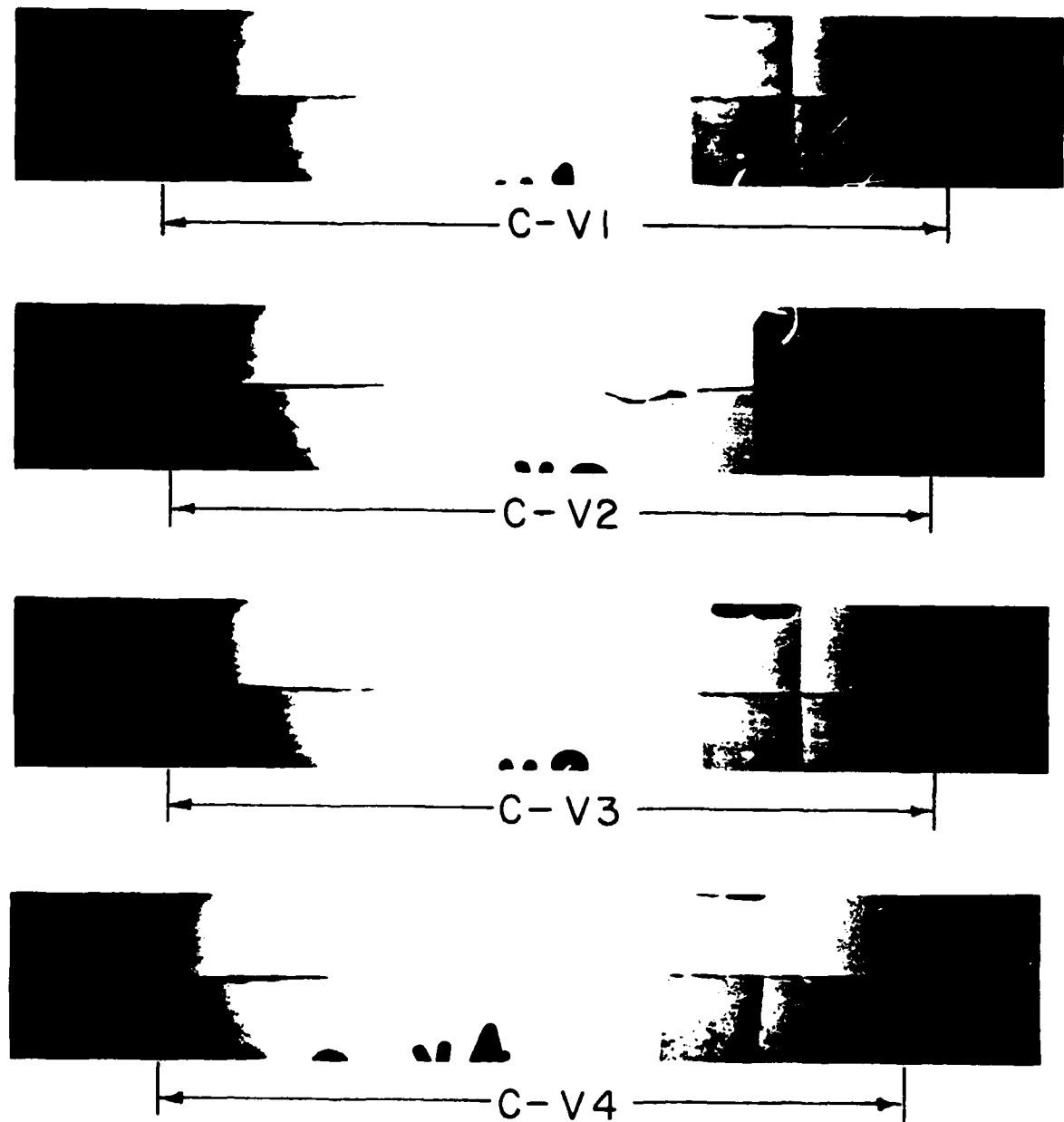
Fig. 15. Radiographic sections of the five-inch
casing weldment #C.

28

B in Fig. 14d. The middle section of the quadrant, shown in Fig.   is the region where the EB undercuts the joint on the outer diameter. Although the radiograph of this section, strip C-V1 in Fig. 15, shows indications of undercuts, it is more readily observed visually. Due to the lack of spatial resolution in the vertical direction, as explained earlier, these undercuts are unresolved in the tomograms. The missed joint regions, A and B, are somewhat distinguishable, based on the uniformity assessment described earlier. As before, we emphasize again that a differencing technique would aid considerably in identifying missed joints.

4.3   Eight-inch Rocket Motor Casing

We next consider the set of weldments contained in the eight inch diameter rocket motor casing. Due to the larger dimensions of this casing, the computer ROIR's were made of the octants, as opposed to the quadrant ROIR's of the previous case. The total cross-sectional tomograms were reconstructed on a 256 x 256 grid with a pixel dimension of 0.83 mm by 0.83 mm. The ROIR tomograms were made using a 0.35 mm x 0.35 mm pixel size.

We begin with the set of tomograms corresponding to Weld #A, on the eight inch casing. The total cross-sectional tomogram is shown in Fig. 16. The octant ROIR's are shown in Figs. 17a to 17h. The first octant, Fig. 17a, is the octant region around 12 o'clock in Fig. 16. The remaining octants are obtained by successively rotating the object cross section (Fig. 16) through 45 deg in a clockwise direction. Rotating the total cross-sectional tomogram in this manner, prior to a ROIR, permits the reconstruction grid location to be the same for all octants. Following the region of interest cross sections from right to

29
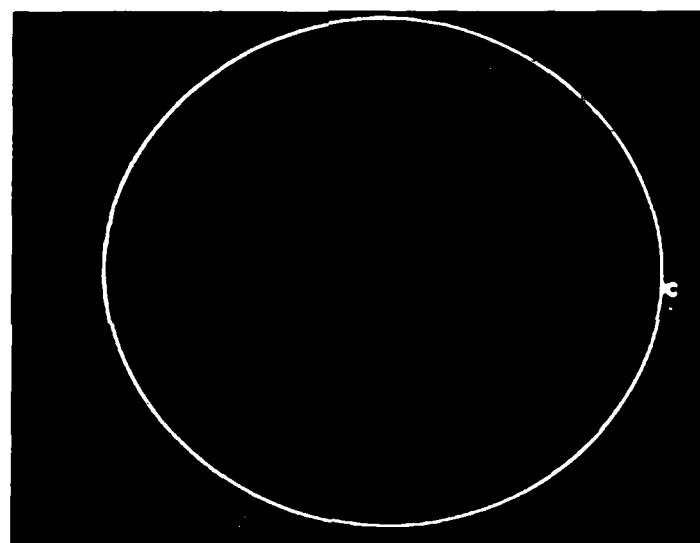
Fig. 16. Cross-sectional tomogram of the eight-inch casing
weldment #A. Source: Ir-192. Grid: 256 x 256.
Pixel dimensions: 0.83 mm x 0.83 mm.

left is equivalent to following the total cross section, counterclockwise, beginning with the octant at the top. In Fig. 18 the ROIR labeling sequence is shown. As shown, each region is slightly larger than an octant, with a slight overlap between consecutive octants on either ends.

As in the five-inch casing, Weld #A represents a good quality weld. The radiograph of this weld is shown in Fig. 19. There are three locations on this radiograph evaluated as a drop-through, i.e., the EB cutting all the way through the back seam, and undercuts. The drop-through was evaluated to be on the inner surface, since visually there is no indication of a weld defect on the outer surface. As mentioned earlier, a radiographic image cannot give the location of a defect relative to the object cross section. Only with other available information, such as obtained from visual inspections, can one provide an educated estimate of the location.

The drop-through and undercut defects were judged minor, and the Weld #A was judged acceptable based on radiographic inspection. These defects are not distinguishable in the tomograms, due to the effect of vertical averaging explained earlier. If the vertical dimensions of the source and detector collimation aperture are reduced, the resultant finer sampling along the vertical would provide a better resolution and detection of such defects.

The next set of tomograms correspond to the weldment #B, which contains regions of lack of fusion and was rewelded once. The total cross-sectional tomogram is shown in Fig. 20, and the octant ROIR's are shown in Figs. 21a to 21h. The corresponding radiograph is shown in Fig. 22. In this set of tomograms some interesting distinctions are
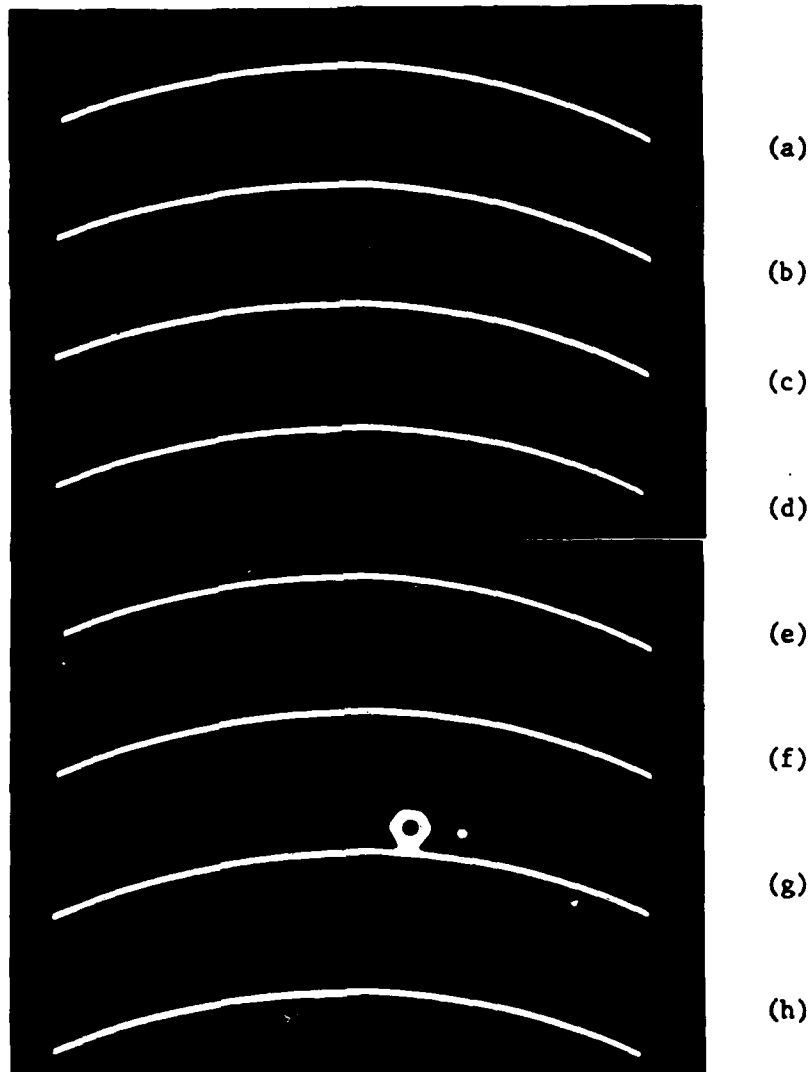
Fig. 17a-h. Eight octant RIOR of the tomogram of Fig. 16. The labeling scheme is as shown in Fig. 18. Each octant RIOR is on a 256 x 256 grid with the pixel dimensions of 0.35 mm by 0.35 mm. The images in 17a through 17h correspond to octants #1 through #8, respectively. The acceptable quality of the weld is indicated by the uniformity of the weld cross-section in all octants.
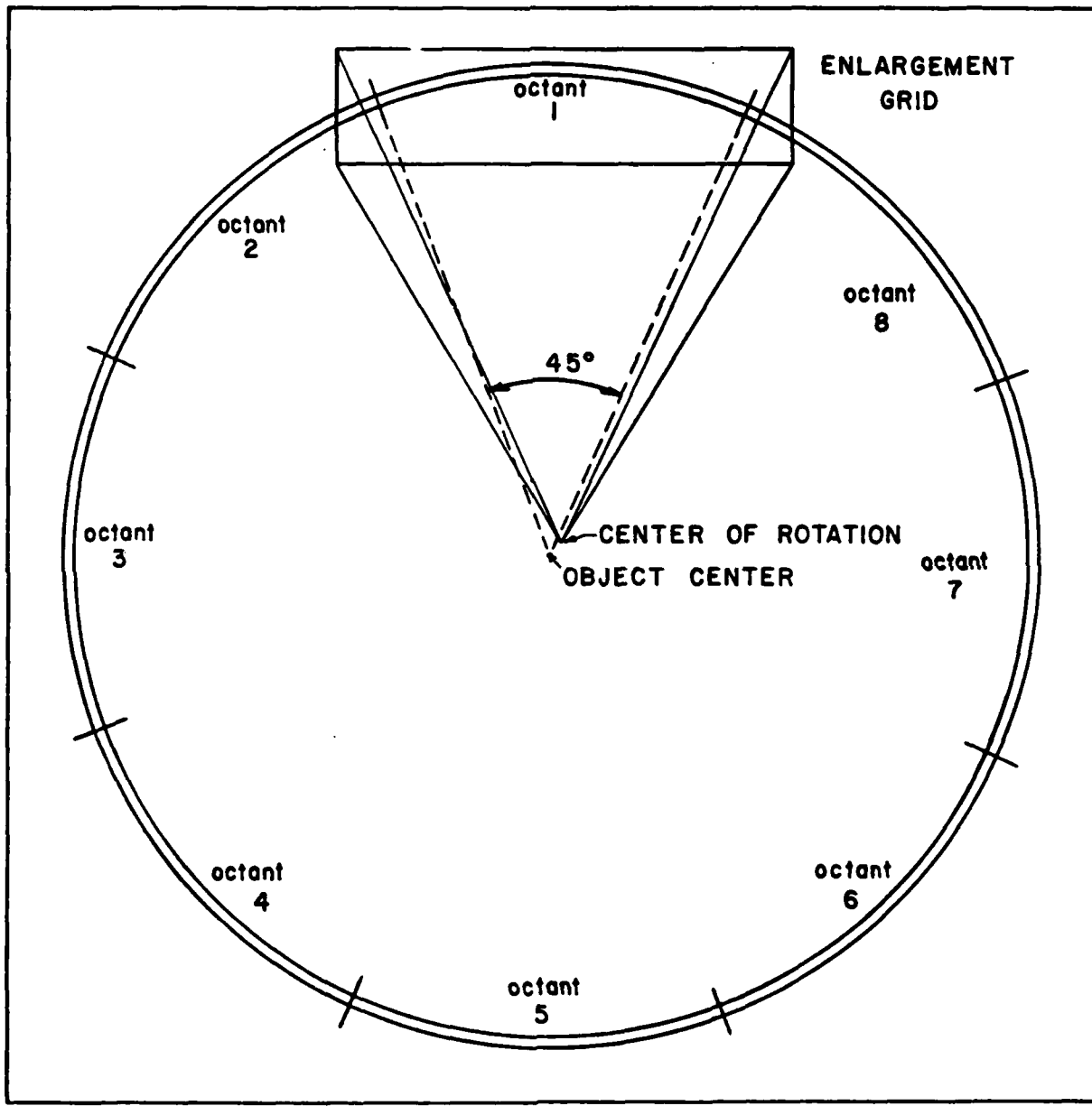
Fig. 18. Labeling scheme for the RIOR tomograms of the eight-inch casing weldments. The octant reconstructions encompass slightly larger than a 45 deg arc; hence, the consecutive octant tomograms have a slight overlap.
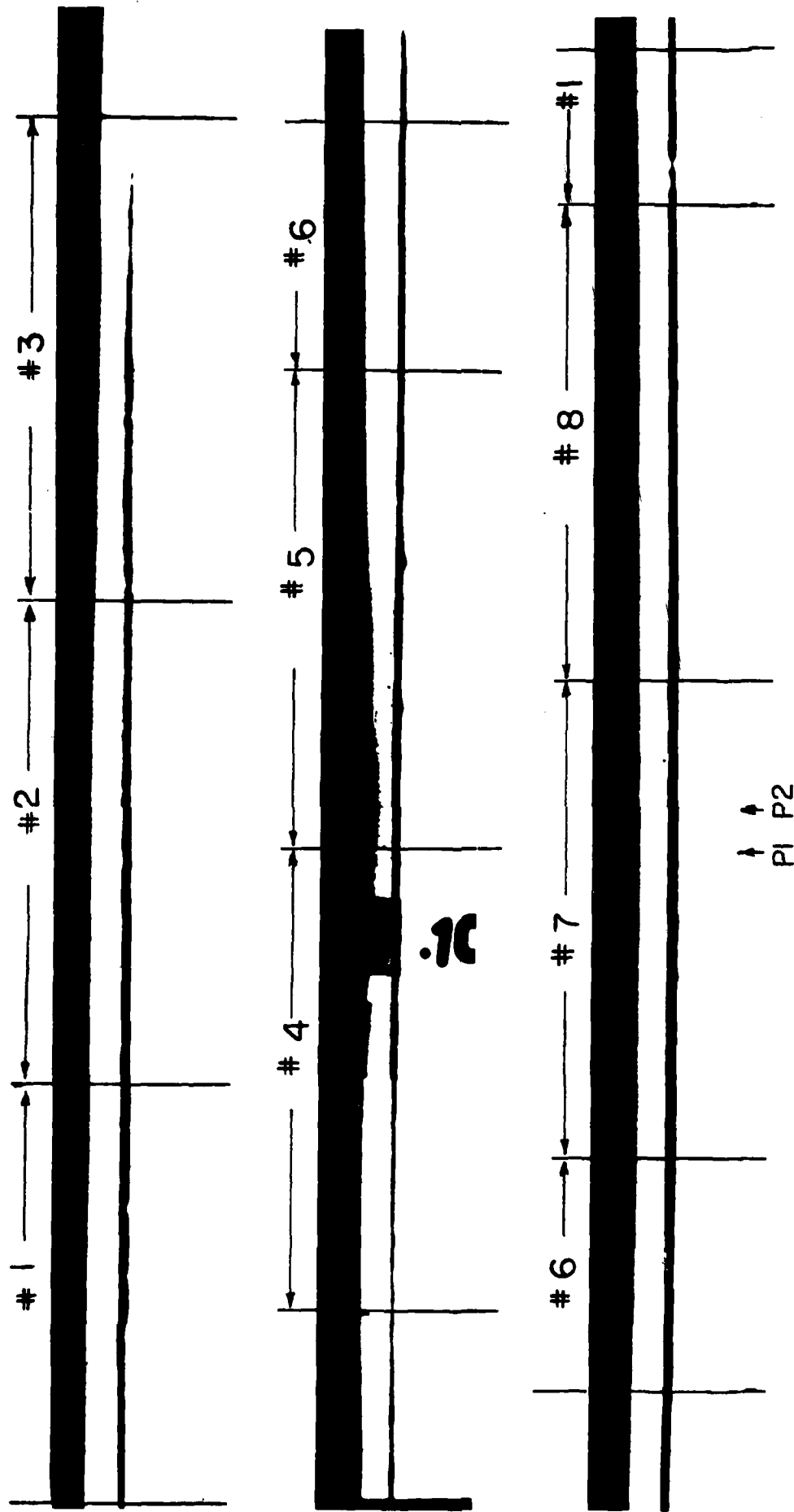
Fig. 19. Radiographic sections of the eight-inch casing. Locations of the reference plug and pin are noted by P_1 and P_2, respectively.

found. The tomogram in Fig. 20, corresponding to the total cross section, shows a thinning of the cross section around the octant #1 region. This is more clearly discerned in Figs. 21a, 21b, and 21h, displaying the cross sections of octants #1, #2, and #8. There is complete fusion in this region, as is evident from the radiograph.

What is not distinguishable in the radiograph, however, is that the reweld pass has gone away from the original weld position, causing the crown formation to move slightly away from the original weld location. Elsewhere, the crown formation is along the original weld. Thus, the thickness of the cross section in these tomograms is noticeably smaller than that in the rest of the octant tomograms. With finer vertical collimation and/or the use of the differencing technique, such shifts in the EB location can be quite readily distinguished.

The second feature of interest is the region of lack of fusion, which was rewelded later, appearing in octant #4. The reweld pass has partially missed the original joint, leaving an indentation along the region on the outer surface. The two weld passes are distinguishable in the radiograph. The lack of contrast in the radiograph obstructs a clear evaluation of this region. It would appear that the region is highly porous or possesses cracks. The tomogram in Fig. 21d, however, shows that only the outer boundary of the cross section is uneven (in comparison to the inner one). This indicates an indentation on the outer surface, rather than cracks or gaps through the weldment.

The last set of tomograms, obtained from the CT examination of EB weldments on rocket motor casings, corresponds to the weldment #C on the eight-inch casing. The total cross-sectional tomogram is shown in Fig. 23, and the octant ROIR's are shown in Figs. 24a to 24h. The radiograph

35
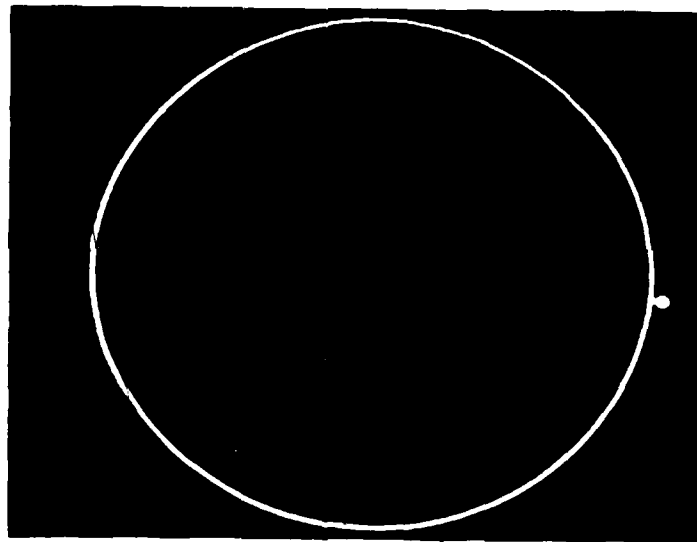
Fig. 20. Cross-sectional tomogram of the eight-inch casing weld #B.
Source: Ir-192. Grid: 256 x 256. Pixel dimensions:
0.83 mm x 0.83 mm.
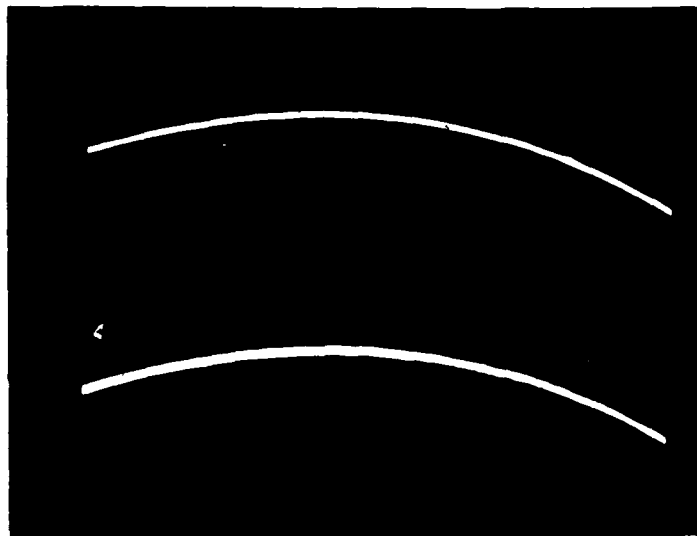
(a) Octant #1
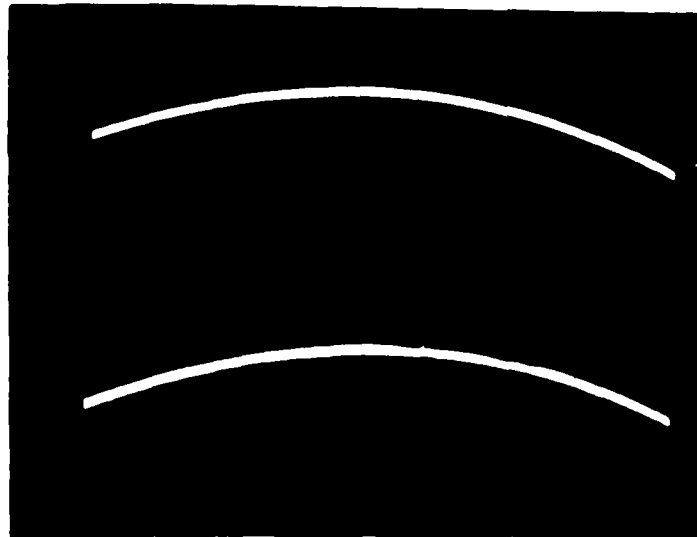
(b) Octant #2

(c) Octant #3

(d) Octant #4

Fig. 21a-d. ROIR tomograms of the Octants #1-#4 of the tomogram
of Fig. 20. The region indicated in 21(d), Octant #4,
corresponds to the location where the reweld pass has
missed the original joint.
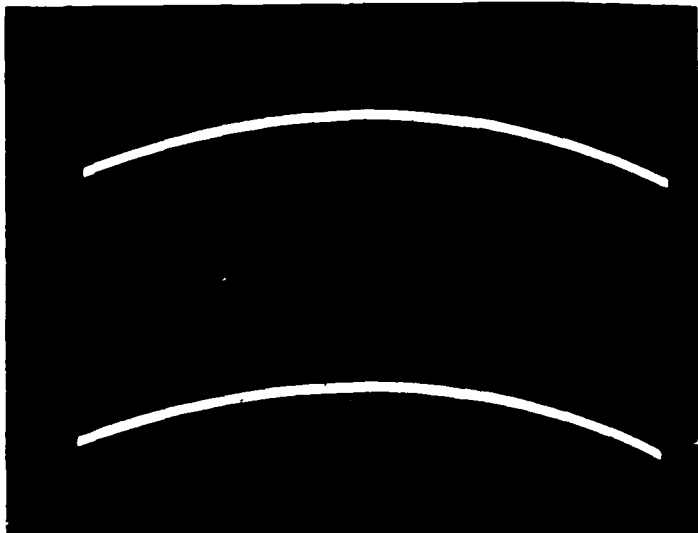
(e) Octant #5
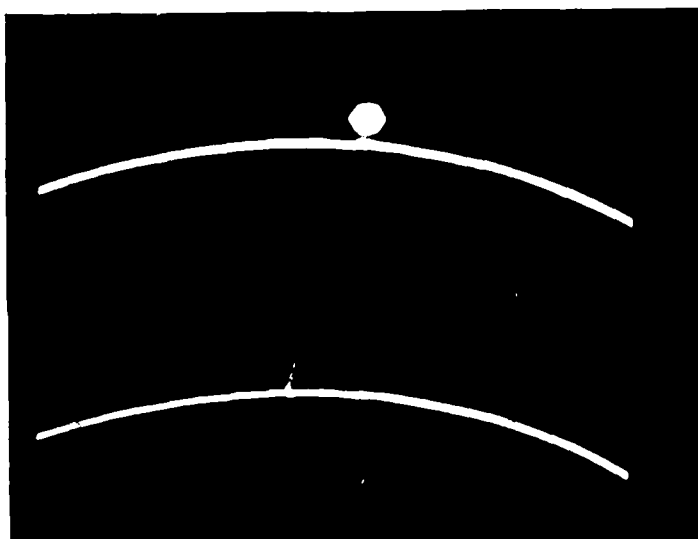
(f) Octant #6
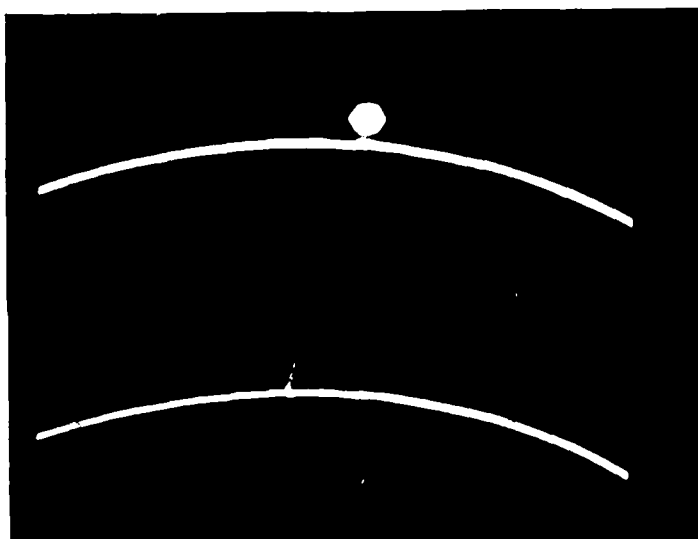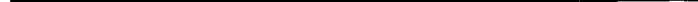
(g) Octant #7

(h) Octant #8

Fig. 21e-h. ROIR tomograms of the Octants #5-#8 of the tomogram
of Fig. 20. The region where the reweld pass misses the
original joint is noticeable in Octant #8, from the
thinning of the cross section.
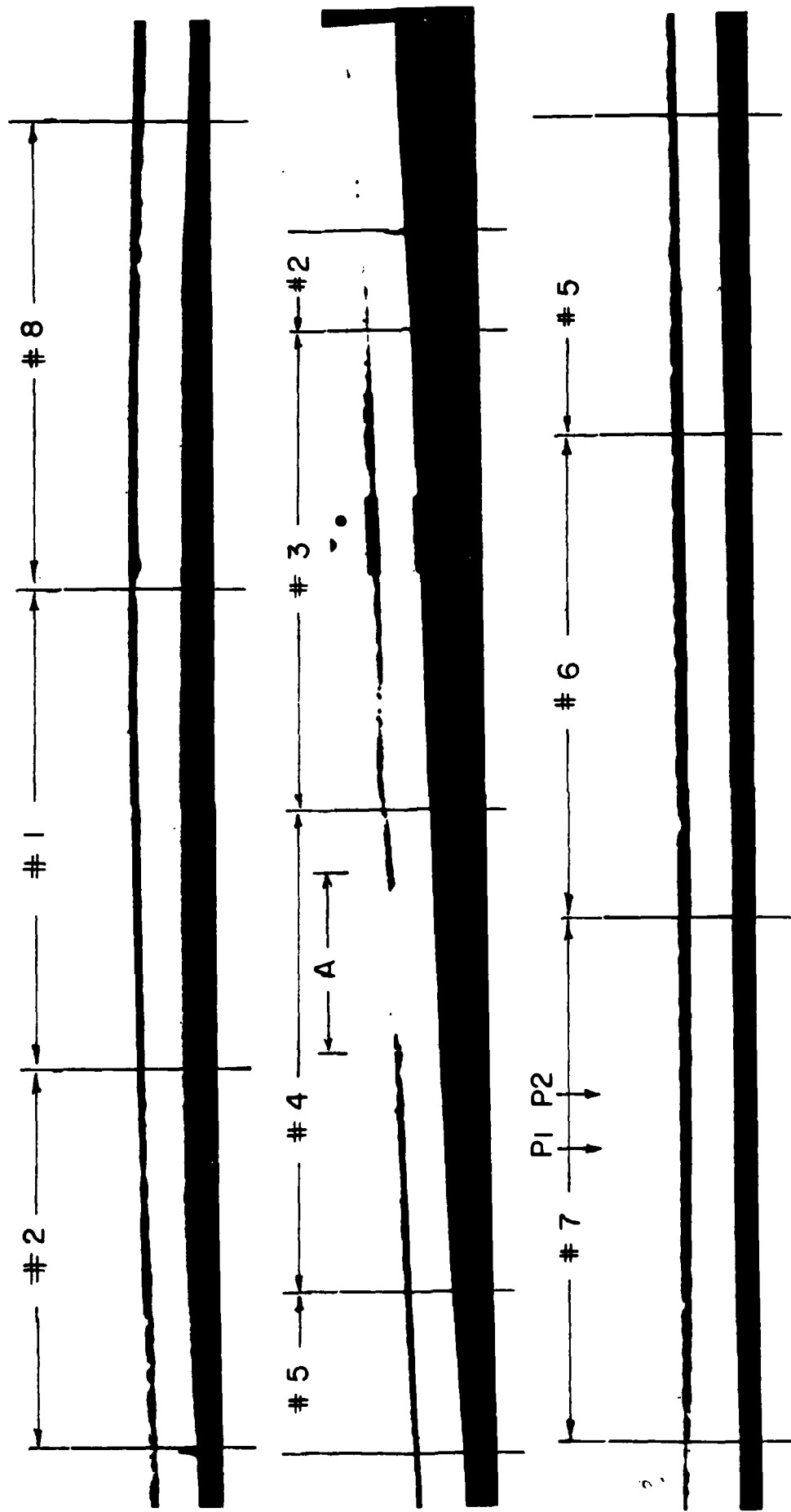
Fig. 22. Radiographic sections of the eight-inch casing weld #B. Region marked A illustrates the difficulty in interpretation of the defect.

of this weldment is shown in Fig. 25. This particular weldment was designed to include lack of fusion and porosity regions. In general, the porosity defects are not prevalent in a vacuum EB welding process. In the present case the porosity was induced by adding material in the weld seam, which vaporized during the welding process. Addition of such material was anticipated to produce fine porosity, however, it produced voids large enough to become gaps in the weldment or cause surface pits.

Certain drawbacks in the interpretation of radiographs are exemplified in this particular case. The locations marked G1, G2 and G3, in the radiograph, are the locations of true gaps in the weldment. These are distinctly resolved in the total cross-sectional tomogram and in the ROIR's of the octants #3 and #4. There are several other regions in the radiograph, which indicate through their contrast level, that these regions are also gaps (e.g., locations marked P_1, P_2 and P_3), or regions of thin metal (i.e. large pores). The location P_1, as indicated in the tomogram of octant #2, is not a gap. It corresponds to indentation or pit formation on both the inner and outer surfaces.

In fact, it is possible to measure the extent of the wall thickness in a tomogram, using a technique which is based on the conservation of mass. Later this technique is discussed when we analyze the weldment in a cast aluminum object. The regions of octants #3 and #4, together, show the regions where surface pitting is present. Corresponding locations in the radiograph leave an ambiguity with regard to their interpretation. In the region marked "pores" in the radiograph, it is not possible to evaluate conclusively a particular location as porous or as a gap.
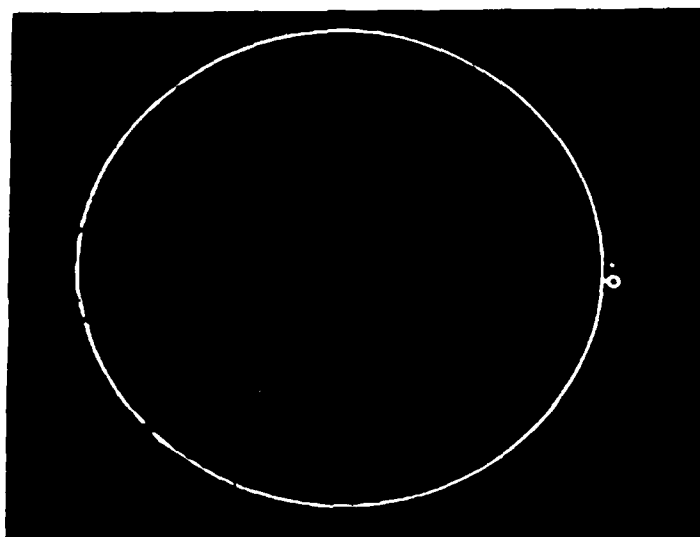
Fig. 23.   Cross-sectional tomogram of the eight-inch casing weld
           #C.   Source: Ir-192.   Grid: 256 x 256. Pixel
   dimensions: 0.83 mm x 0.83 mm.   Regions of large
           pores or cracks are visible on the left boundary.
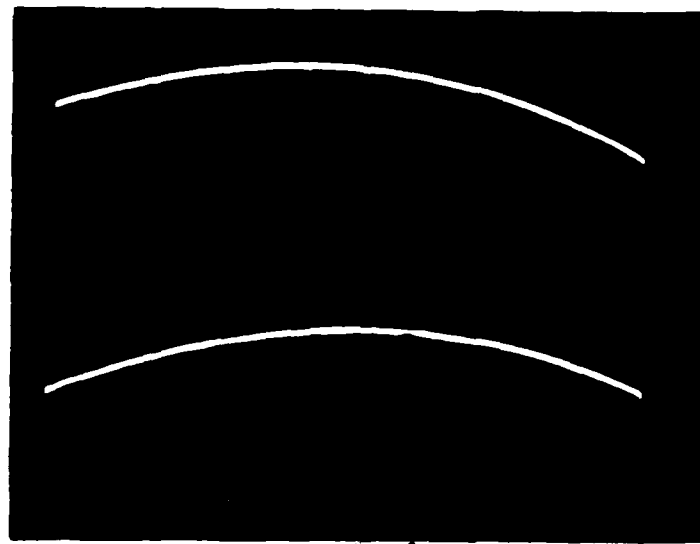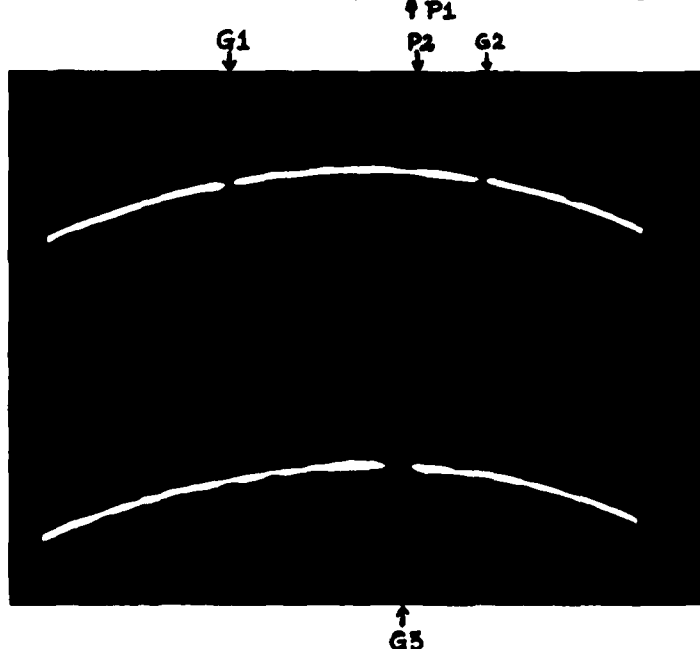
Fig. 24a-d. ROIR tomograms of the Octants #1-#4 of the tomogram of Fig. 23. Locations marked G_1, G_2 and G_3 are true gaps. Location P_1 in Octant #2 is the location of indentation interpreted as a gap in the radiographic image.
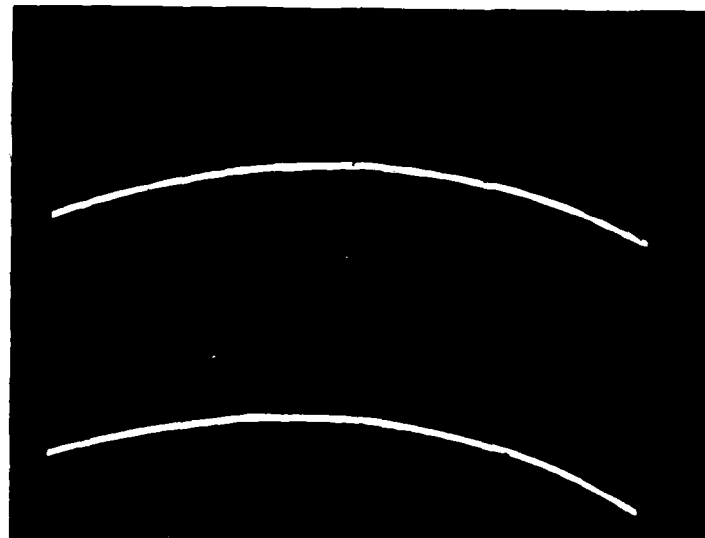
(e)   Octant #5
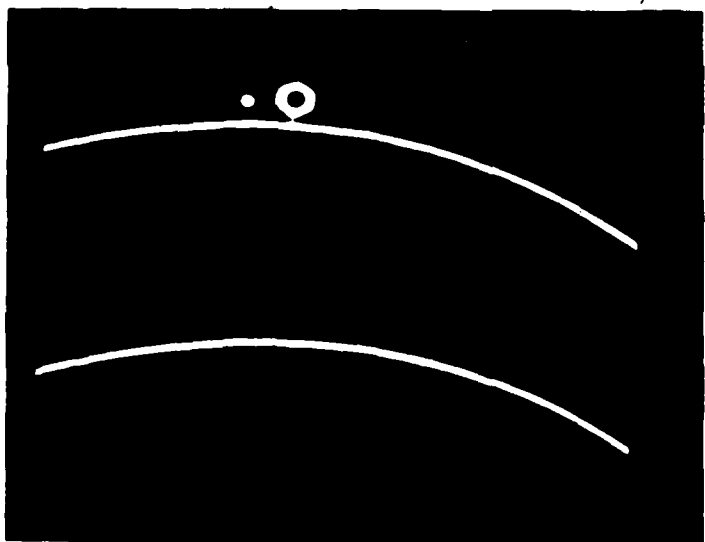
(f)   Octant #6

(g)   Octant #7

(h)   Octant #8

Fig. 24e-h.   ROIR tomograms of the Octants #5-#8 of the tomogram
              of Fig. 23.

Fig. 25. Radiographic sections of the eight-inch casing weld #C.

In tomography, by studying the cross-sectional thicknesses, the defects such as surface pits are readily distinguishable from clear gaps. In radiographic images, the regions of thin wall thicknesses can often be misinterpreted as gaps or regions of porosity.

As we have observed previously, the tomographic detection of features of certain extents strongly depends on various tomographic parameters; for example, collimation in the horizontal and vertical directions. The nature of application, therefore, dictates the choice of tomographic parameters. Fortunately, the parametric range in tomography covers a wide range. It is possible, therefore, to obtain a high resolution of features of interest, through tomographic examinations. To examine how the spatial resolution depends on the tomographic parameters, we discuss below a parametric study of the spatial resolution.

4.3.1 Parametric Investigation of the Eight-inch Casing. The comprehensive data, obtained for weldment #C of the eight-inch casing, were used for studying the degree of spatial resolution as a function of the number of angular views and the ray spacings in the photon fan beam. The exposure time, the source-detector collimations and the source type were left unchanged. A set of six tomograms was reconstructed using pairing of 400 views, 200 views, and 133 views with ray spacings of 0.065 deg, 0.13 deg and 0.195 deg. These ray spacings correspond to a sampling extent of 0.69 mm, 1.38 mm, and 2.1 mm, respectively, at the object center of rotation. These tomograms, shown in Figs. 26a to 26e are reconstructed on the same grid and pixel specifications as for the comprehensive tomogram shown in Fig. 23.

We first consider the influence of the reduced number of views, by

45

comparing the tomograms in Fig. 23 and Fig. 26, with 400 angular views and 133 angular views, respectively. In both these cases, the ray spacing is maintained at 0.065 deg (0.69 mm). As far as the resolution of the gaps and the nonuniformity of the weld cross section is concerned, the reduction in the number of angular views has not lowered the resolution by any significant amount.

There are several factors contributing to the degree of spatial resolution. In particular, the sampling size and the amount of sampling dictate the degree of resolution.

The source and the detector collimation apertures define the sampling volume, and ultimately dictate the degree of spatial resolution. Ray spacings, defined as the spacing between two consecutive detector positions, and the number of angular views dictate the amount of sampling. The image quality, in addition to these, also depends upon the manner in which the different regions of the object cross section get sampled.

It is obvious from the fan beam geometry that an object region closer to the source, i.e. the apex of the fan, is examined more finely than a region farther away from the apex. In addition, any particular volume element (voxel) receives a nonuniform degree of sampling as the object rotates through 360 deg. To understand this nonuniform nature of sampling, consider two regions of the fan beam; one region around the axis of the fan (i.e. around the ray passing through the center of rotation) and the other region around the edge of the fan. A voxel situated closer to the boundary of the object, will experience a larger degree of sampling in the fan edge region in comparison to the sampling received in the axial region. In particular, if the object boundary is a regular, symmetric geometrical shape, such as a circle, the boundary voxels will be oversampled in the

46
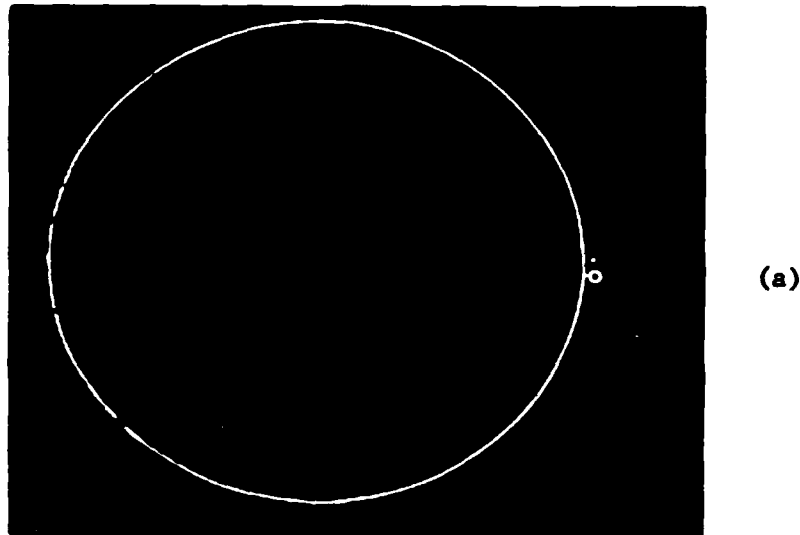
(a)

Fig. 26. Tomograms of the eight-inch casing weld #C, reconstructed
with different combinations of the number of angular views and
ray spacings. Fig. 23 is the tomogram of the comprehensive case
with 400 views and a 0.69 mm ray spacing. The sequences of the
tomograms shown are reconstructed using the combinations (a)
133 views and 0.69 mm ray spacing, (b) 400 views and 1.38 mm ray
spacing, (c) 400 views and 2.07 mm ray spacing, (d) 200 views
and 1.38 mm ray spacing, and (e) 133 views and 2.07 mm ray
spacing. Ray spacing is measured at the center of rotation of
the object.
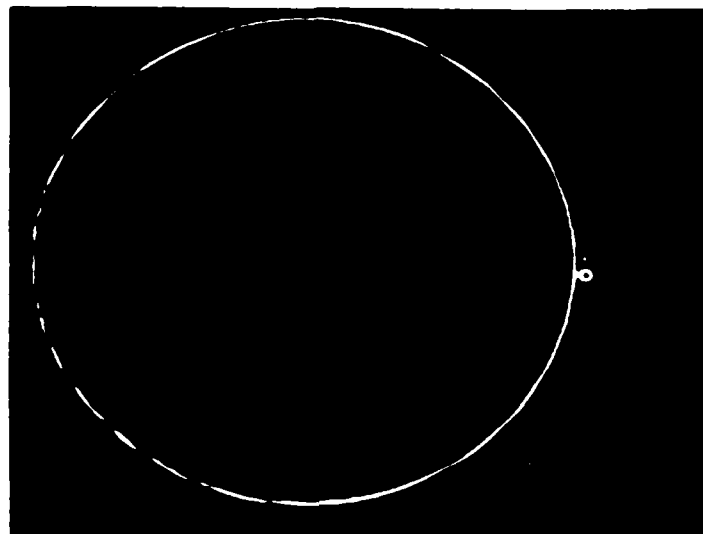
Figure 26b
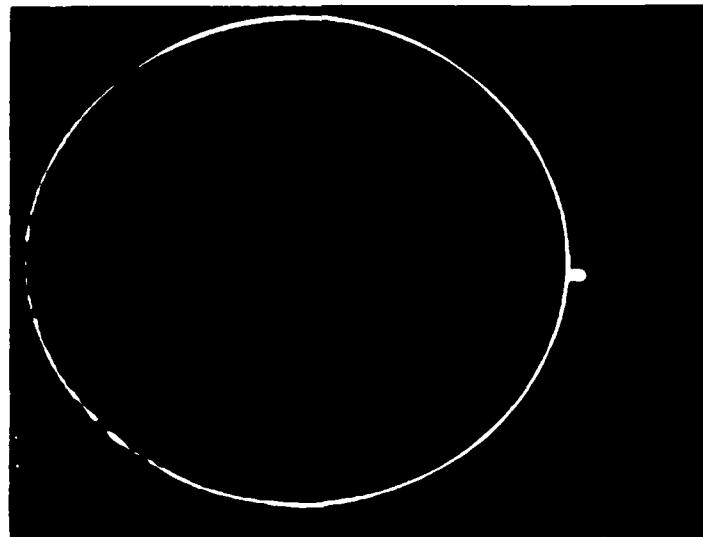
Figure 26c
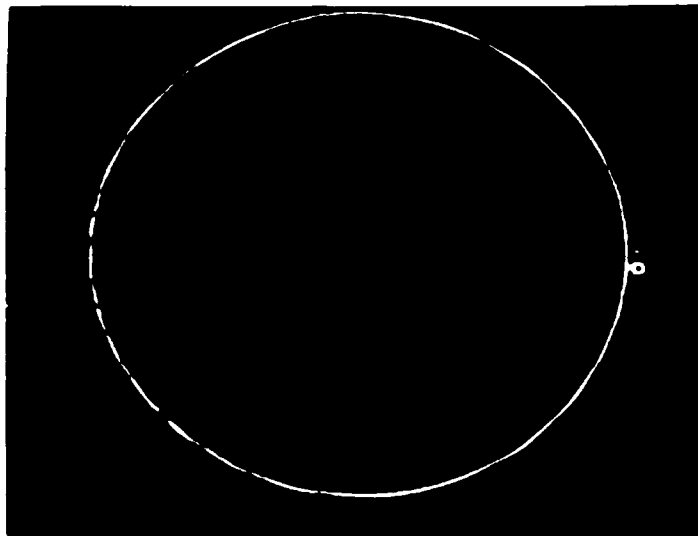
Figure 26d

Figure 26e

49
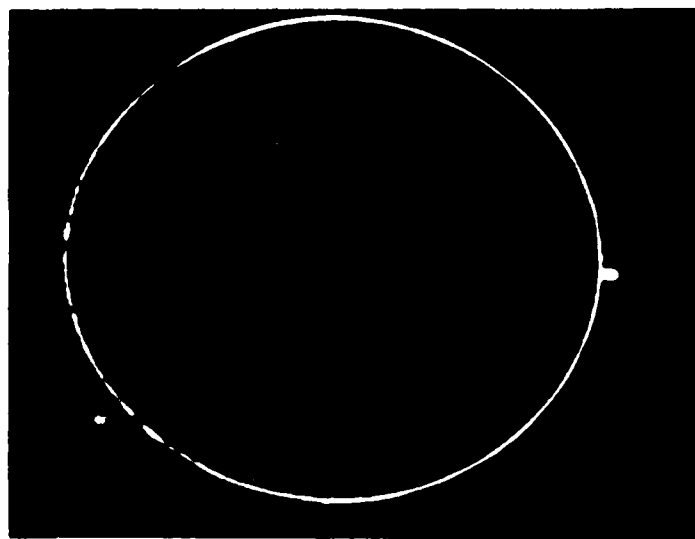
fan edge region. Oversampling serves to improve the statistical quality of the corresponding data. On the other hand, if the object boundary is irregular, the boundary voxels may not receive any additional sampling in the fan edge region.

The increased ray spacing and/or reduced number of views leads to undersampling and degrades spatial resolution. Increased sampling volume implies a coarse sampling and poor resolution. Increasing the number of views and/or reducing the ray spacings indefinitely does not necessarily imply an improved resolution. When the spacing between two successive angular views become smaller than or comparable to the sampling volume on the ray spacing in the fan beam, any further increase in the number of views results simply in oversampling.

The fact that the spatial resolution in the present case did not degrade significantly (at least visually) when the number of views were reduced, is partly due to the shape of the object and the manner in which object is sampled. Since the object is cylindrical, coarser sampling of the voxels around the axis, introduced by the smaller number of views alone, is apparently compensated by the larger sampling in the fan edge region, as explained earlier. The effect of the reduced number of views (i.e. undersampling) would have been more pronounced if the object boundary was irregular and nonsymmetric.

The influence of the ray spacings on spatial resolution is seen by comparing the two tomograms shown in Figs. 26b and 26c. These cases correspond to a ray spacing of 0.13 deg (1.38 mm) and 0.195 deg (2.1 mm), respectively, with 400 angular views. Because of the coarser sampling of the object, as compared to the comprehensive case, the definition of the object cross

50

section in these cases is noticeably more uneven. Spatial resolution is degraded as the sampling extent increases. As can be seen from the tomograms, the poor quality of the image due to lowered spatial resolution, may introduce ambiguity in feature detection and identification.

The reference plug in the tomograms provides a basis for quick comparison of these three cases. As the ray spacing is doubled, the hexagonal shape of the plug is poorly resolved in Fig. 26b. A further increase in the ray spacing, as shown in Fig. 26c, leaves the shape unresolved and barely resolves the hole in the center of the plug.

The effect of the angular views on spatial resolution, in comparison to the ray spacings, is not so drastic. This can be observed from Fig. 26d and Fig. 26e, where the number of views are 200 and 133, respectively. Comparing these with the tomograms reconstructed using the corresponding values of the ray spacing, but 400 angular views (Figs. 26b and 26c), show that there is not much difference in the spatial resolution. As mentioned earlier, the circular symmetry permits an examination with a lesser number of views, without suffering significant degradation of the spatial resolution.

The influence of these tomographic parameters may be summarized as follows. The degree of spatial resolution obtainable depends on the sampling volume, the ray spacings in a fan beam, and the angular views. The choice of these parameters dictates the amount of data collected. An indiscriminate increase in the number of views and/or rays results simply in oversampling of the object, without increasing the spatial resolution. On the other hand, undersampling can lead to artifacts and inadequate definition features.

The other tomographic parameters influence the spatial resolution in a different manner. The resolution of mass densities in an object composition depends on the differential attenuation experienced by the incident photon beam. As described in Section 2, the attenuation suffered by the photon beam depends not only on the object composition, (i.e. the Z values) but also the energy of the photons. At higher photon energies, the attenuation is less. This implies that small differences in the mass densities are difficult to resolve at higher photon energies. This is particularly important when the object extent is small compared to the attenuation length. An attenuation length for a given material, at a given incident photon energy, is the length over which the beam intensity drops by a factor exp (-1), or reduces to approximately 37 percent of the initial intensity. The choice of the source is, therefore, dictated by the object characteristics such as its composition and size.

The source strength and/or the exposure time becomes significant in the consideration of the signal-to-noise ratio. Since photon flux from a random source obeys Poisson's statistics (2), the counting statistics are improved at higher photon counts. This may be achieved by using higher strength sources or larger exposure times or a combination of these. Although the counting statistics are improved by obtaining a larger transmitted flux, the magnitude of the scattered radiation also increases. The effect of the scattered radiation is to introduce artifacts in the image or, equivalently, reduce the signal-to-noise ratio. The scattering effects can be substantially reduced by collimation of the detectors and proper detector shielding.

To summarize, the degree of spatial resolution is ultimately limited by the source-detector geometry, defined by the collimation of the source and the detector. Collimation has further significance in that it lowers the effects of scattering, thereby improving the signal-to-noise ratio. The source characteristics and the choice of exposure times depend on the object characteristics.

4.4   Aluminum Casting

The case of weldments in an aluminum casting differs from the previous case in several ways. First, the type of weldment is different. The weldments were made using a standard heliarc welding process, and are significantly larger in extent compared to the EB weldments. Secondly, in contrast to the thin cylindrical shells of the previous case, the casting is extended, non-symmetric and massive. Such object sizes and shapes would cause difficulties with regard to radiographic imaging and analysis. Even though such objects can be radiographed, the image does not provide any information regarding a defect orientation or location.

In radiographs of the steel rocket motor casing, since steel attenuates x-rays significantly more than air, a high contrast was possible between air and steel. In contrast, aluminum has a lower atomic number (Z) and has one-third the density of steel. Consequently, the relative contrast between air and aluminum is not as high in radiographic imaging.

Furthermore, depending on the size of the object, the completion of a radiographic image may require relatively long periods of time. In objects such as the one examined here, several radiographs may be required

53
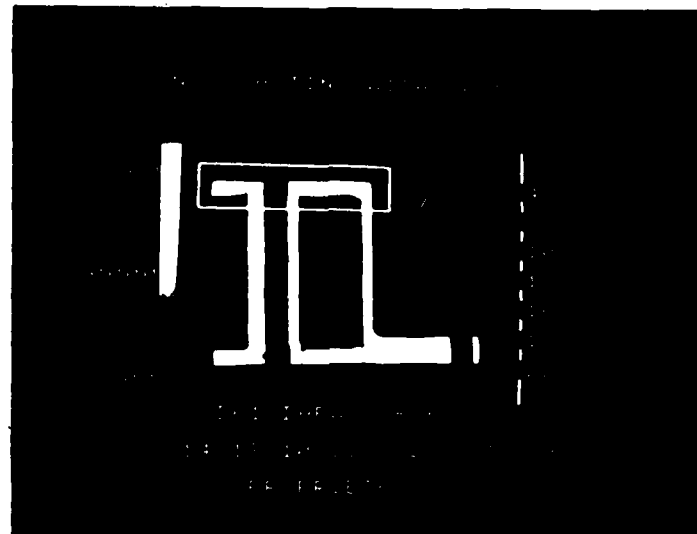
Fig. 27. Cross-sectional tomogram of the cast aluminum object, through the plane shown in Fig. 5a and 5b. The density range is marked on the left. The rectangular grid at the top of the object cross section in the region reconstructed for quantitative evaluation. Source: Ir-192. Grid: 128 by 128. Pixel dimensions: 1.06 mm x 1.06 mm. Number of views: 600. Ray spacing: 0.69 mm.

to study each weldment individually. The use of CT methods easily permits not only the detection of a defect but also information on its location and orientation within the object.

The object examined here was described earlier in the section. It was tomographically examined along the cross section marked in Figs. 5a and 5b. Only one cross section of this object was examined. The corresponding tomogram of the total cross section is shown in Fig. 27. The rectangular area at the top of the cross-sectional image shows the region of interest reconstructed on a finer pixel size. The tomogram in Fig. 27 was reconstructed using a 128 x 128 grid with a pixel size of 1.06 mm x 1.06 mm. The ROIR tomogram of the area at the top was made on a 256 x 64 grid with pixel dimensions of 0.35 mm x 0.35 mm. This tomogram is shown in Fig. 28a. The CT examination was made using 600 views and a ray spacing of 0.065 deg. The detector collimation aperture was 2 mm (height) by 1.5 mm (width), as in the earlier cases.

The two vertical regions, on the left in Fig. 27, correspond to the cross section of the aluminum cylinder, welded to the aluminum bracket at the top and the bottom ends. The top and bottom plates of the bracket are also welded to a side plate. Even on the larger pixel size used in the reconstruction of this tomogram, the defective nature of weldments on the cylinder is evident. At the location of the weldment, appearance of low density (darker) areas indicate the presence of defects such as lack of fusion, cracks and porosity. The ROIR tomogram of Fig. 28a displays these areas more clearly.

Examining the tomogram in Fig. 28a, there are four regions of lowered density, marked R1 to R4. One location of the weldment is at the lower end

55
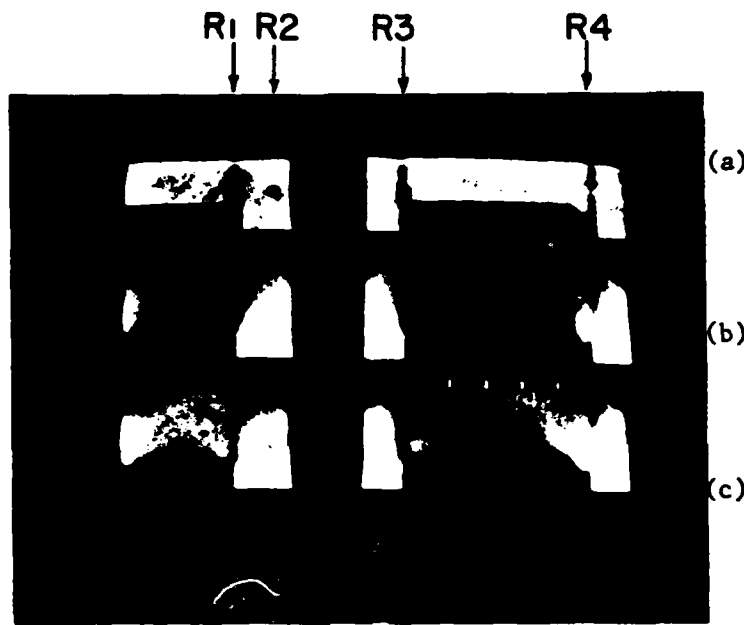
Fig. 28. ROIR tomograms of the section marked in Fig. 27.
(a) Reconstruction of the region of interest using the
entire data set, (b) reconstruction with data correspond-
ing to a 90 deg partial view, and (c) reconstruction
with data corresponding to a 120 deg partial view. Each
ROIR tomogram is reconstructed on a 256 x 64 grid with
0.35 mm x 0.35 mm pixel dimensions. Locations R_1, R_3

and R_4 mark the defective regions of the weldment. R_2

is the location within the object of a casting defect
within the object.

of the region R1. A lack of fusion area as well as a cavity is visible. The weldment cross section is perpendicular to the object cross section shown in this tomogram. The locations R1 and R3 correspond to the weldment of the cylinder, whereas region R4 corresponds to the location where the top plate is welded to the side plate of the bracket. The regions of the weldment on the cylinder, R1 and R3, both exhibit voids or lack of fusion.

Since a tomogram is essentially a map of the mass density distribution within an object cross section, it is easy to study quantitatively the variation in mass densities. From the information on the mass distribution, it is possible to calculate extents of features such as voids.

The capability of CT for accurately imaging features is demonstrated below, where the extents of the voids in regions R1, R2 and R3 are evaluated. An illustration of the mass distribution, across any line in a tomogram, is displayed in Fig. 29a. The trace of the mass density is taken along a line, which approximately passes through the center of the void in the region R2. Regions R1 to R4 are clearly evident in this mass profile. The flat plateau between the locations R3 and R4 indicates the uniform mass distribution of the aluminum background. In relation to this homogeneous background, it is possible to quantitatively evaluate the amount of mass missing from the regions where the profile values fall below the uniform background. A completely homogeneous object, in principle, would display a constant value in the mass profile. Thus, for a reasonably homogeneous object composition, any variation in the mass profile is indicative of the presence of anomalies and/or image artifacts. A slight variation in the plateau, between the points R3 and R4, is due to
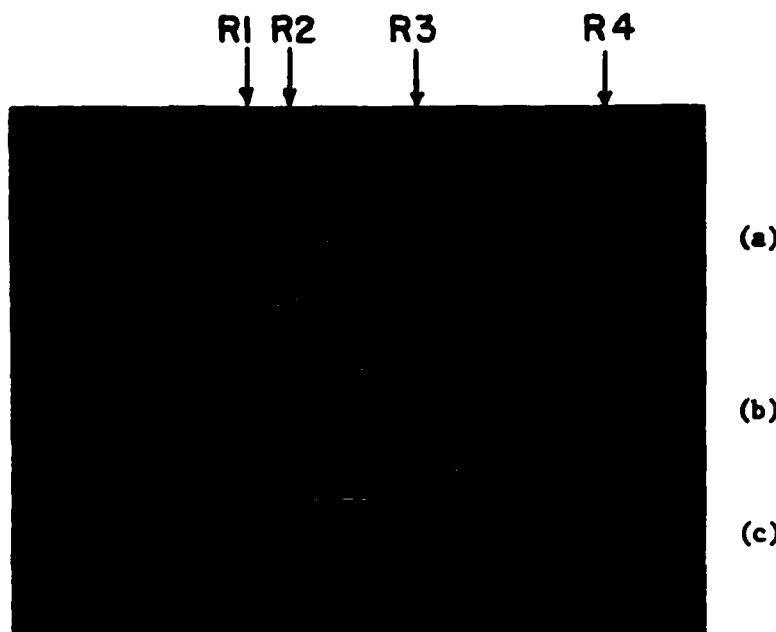
Fig. 29. Example of mass distribution profiles used for
quantitative evaluation of the extent of defects.
One profile is shown for each of the ROIR tomo-
grams of Fig. 28.

circular artifacts. The influence of the circular artifacts is more pronounced in the region left of R1.

A series of mass profiles were traced, starting from a line slightly beyond the top of the void in region R2. In each trace the value of the homogeneous background density was evaluated by averaging the mass profile across the plateau region. By integrating the profile over the regions where it significantly deviates from constancy, the amount of missing mass was estimated, in reference to the homogeneous background value. If it is assumed that the lowered value of the mass, (i.e. the amount of missing mass), in a particular region is entirely due to air voids, the dimension of the region occupied by air can be computed. In this manner, a quantitative estimate of the void extents is obtained. We note that, although a feature smaller than the sampling volume cannot be totally resolved, the method of conservation of mass used here gives quite an accurate assessment of the size.

The extents of the regions R1, R2, and R3, calculated from the analysis of the mass profiles, are shown in Fig. 30. The dimensions are plotted as a function of the distance along the vertical, starting from the top of the defects and continuing downwards.

The void in the region R2 is within the aluminum cylinder and is a defect in the casting. Identification and evaluation of this pore reveals the advantages of the CT methods. The usual methods used for the inspection of such weldments, for example the dye penetration technique, would not provide any information on the homogeneity of the object itself. In CT examinations, in addition to the weld joints, the entire object is evaluated quantitatively without any additional effort. Accordingly, tomography is well suited for inspections of extended, non-symmetric, massive objects.

59
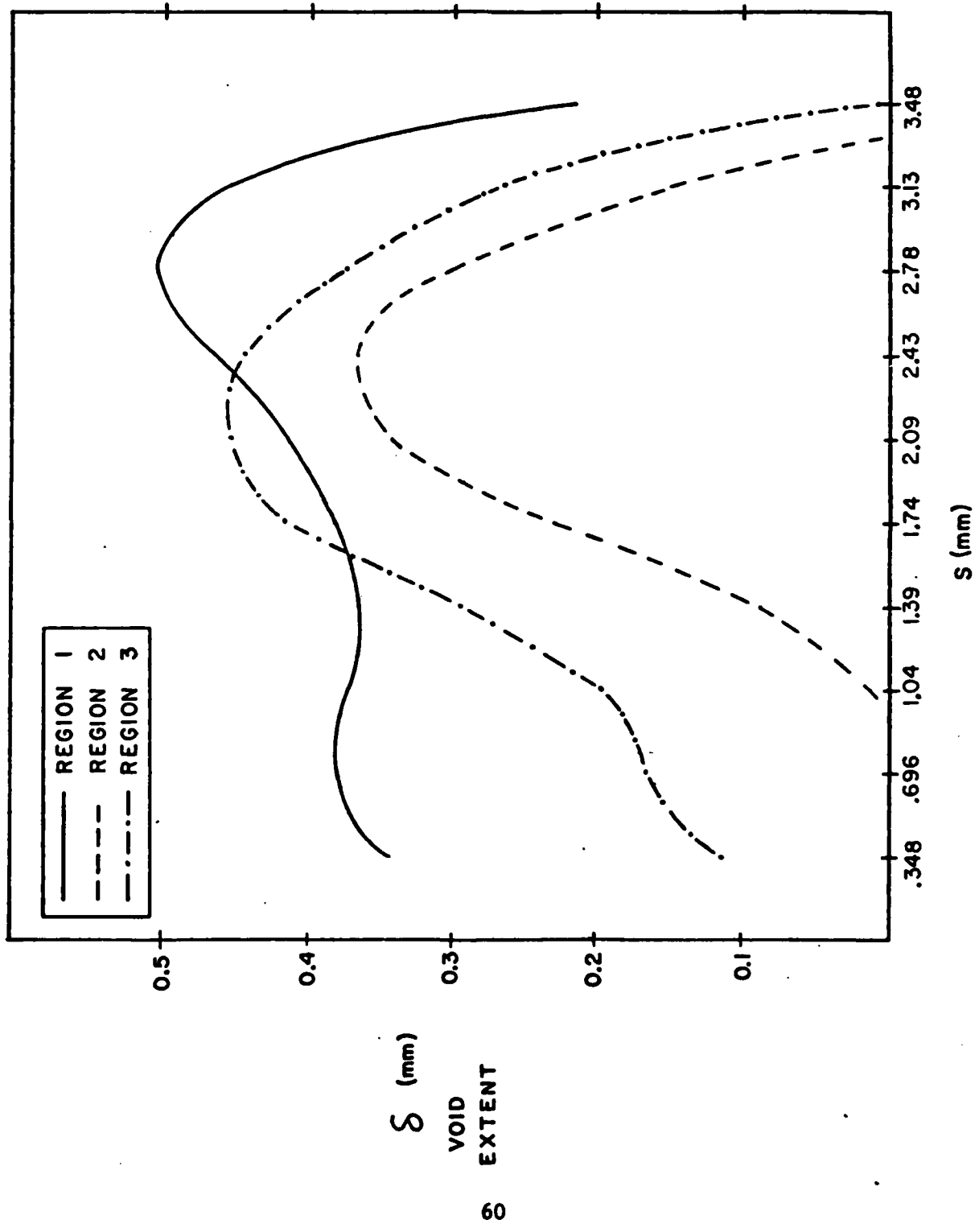
FIG. 30. LOCATION OF THE MASS PROFILE
THROUGH THE VOID

S (mm)

δ (mm)

VOID
EXTENT

REGION 1
REGION 2
REGION 3

Before continuing to the next topic of discussion, we note that the vertical traces in the regions R1, R3 and R4, are artifacts arising from what is known as edge effect. In CT scanning, such artifacts arise along the boundaries across which a sharp density contrast exists. The edge effect reflects the response of a detector as it samples such a boundary. These artifacts can be reduced by finer sampling and corrective algorithms. The evaluation of the feature extents, described above, has included the consideration of the contribution of these artifacts.

4.4.1 <u>Limited View Reconstruction of Aluminum Casting</u>. This particular sample was also used for a study of the limited view tomography. In situations where the object dimensions are so large that a typical 360 deg tomographic scan is prohibited, the object may still be examined through a limited angular view scan. Although a limited view examination obtains only a limited amount of information, it may suffice to indicate the presence of some defective features.

The ROIR tomograms corresponding to a 90 deg scan and a 120 deg scan are shown in Figs. 28b and 28c, respectively. Since only a limited amount of data is obtained in such scans, the reconstructed image lacks definition. For example, the object definition along the horizontal, i. e., the cross section of the upper plate, is almost totally unresolved, and its boundaries are completely undefined. This is because the partial view scan was performed around a direction perpendicular to this plate. The details along the perpendicular direction are better defined; for example, the cylinder and the side plate cross sections.

With 120 deg data, we observe that the voids in the weldment, as well as the pore in the casting, are reasonably well resolved. The mass profile in Fig. 29c displays the degree of this resolution. Similarly, a reasonably good degree of resolution is evident, even when the scan is limited to a 90 deg view.

The image quality provided by these limited view scans indicates that, in many situations involving extended objects, features of certain sizes and orientations can be resolved with less than complete angular sampling of the object. In particular, if the features are oriented in the general scan direction, there is a higher probability of their resolution. Features which lie almost perpendicular to the scan direction offer a poor chance of detection, because of the limited nature of the data.

4.5 Thin Aluminum Plates.

The final set of weldments corresponds to the set of plate weldments obtained from the U.S. Air Force, Kelly Supply Depot, San Antonio, Texas. These are samples of standard inert gas weldments made on thin plates. The plates are sections of special alloy panels typically used in the construction of thin-walled aircraft body components. The weld thickness range between 0.9 mm and 3.5 mm. The typical defects in these weldments are porosity and inclusions.

The tomograms of these weldments are shown in Figs. 31a, 32a, and 33a, with the corresponding radiographs in Figs. 31b, 32b, and 33b. The extent of the pores and inclusions is submillimetric, as can be seen from the radiographs. In radiographs, darker regions correspond to higher densities and the lower density regions are brighter in contrast. The opposite is true for the tomograms.

The tomographic scans were made using 600 angular views, a ray spacing of 0.04 deg and an exposure time of 0.2 seconds. The detector collimation aperture was 1.5 mm (width) by 2.00 (height). The effective sampling extent at the center of rotation of the object was approximately 0.48 mm. The tomograms shown display three consecutive sections of the welds. Essentially these are three ROIR's for a given weld, displayed on a single frame. The tomograms were reconstructed on a 0.28 mm x 0.28 mm pixel size.

The tomogram shown in Fig. 31a is the cross section of the thinnest weldment. As shown in Fig. 31b, the corresponding radiograph shows a region of linear porosity, which approximately corresponds to the central region in the tomogram. The porosity is unresolved in the tomogram, presumably due to (1) the dimensions of the individual pores and (2) the effect of vertical averaging. The tomograms in Figs. 32a and 33a display a structure in the weld cross section, indicating an inhomogeneous character of the cross section. These are several regions which can be identified as pores or inclusions. The presence of circular artifacts, however, prohibits a confident evaluation.

There are several ways in which the resolution can be improved for weldments and the defects of this type. The use of a low energy source, very fine collimation of the detectors and various data smoothing and error correction algorithms, would improve the visibility of such small features.

63
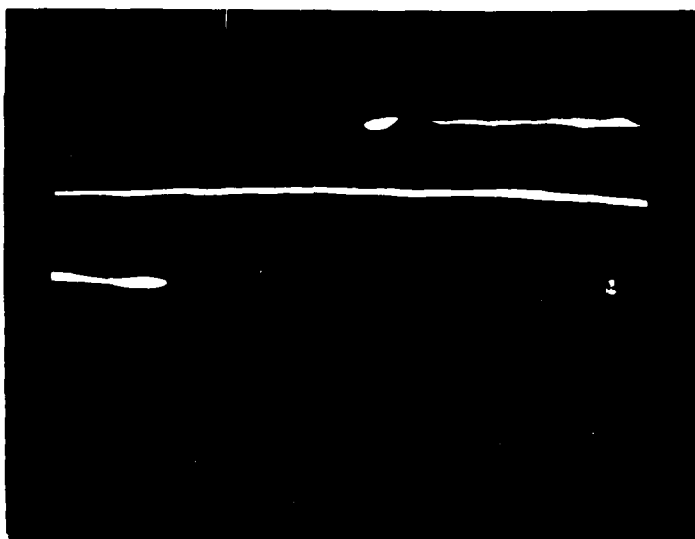
(a)

(b)

Fig. 31. (a) Tomogram of the plate weldment obtained from
the U. S. Air Force, Kelly Supply Depot. The total
cross-section is divided into three RIOR tomograms,
shown collectively on a single display. Each RIOR
tomogram is on a 256 x 45 grid with a 0.28 mm x 0.28
mm pixel size. Source: Ir-192. Exposure: 0.2 sec.
Number of views: 600. Ray spacings: 0.48 mm.
(b) The corresponding radiograph.

(a)
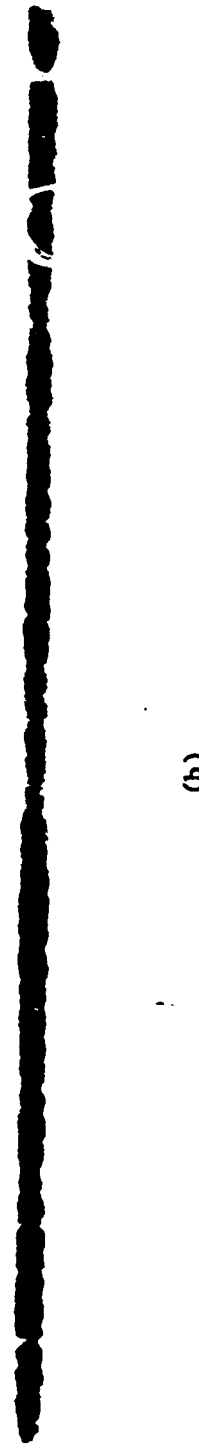
(b)

Fig. 32. (a) ROIR tomograms of the second plate weldment obtained from the U. S. Air Force, Kelly Supply Depot, reconstructed with the same scan parameters as in Fig. 31. (b) The corresponding radiograph.
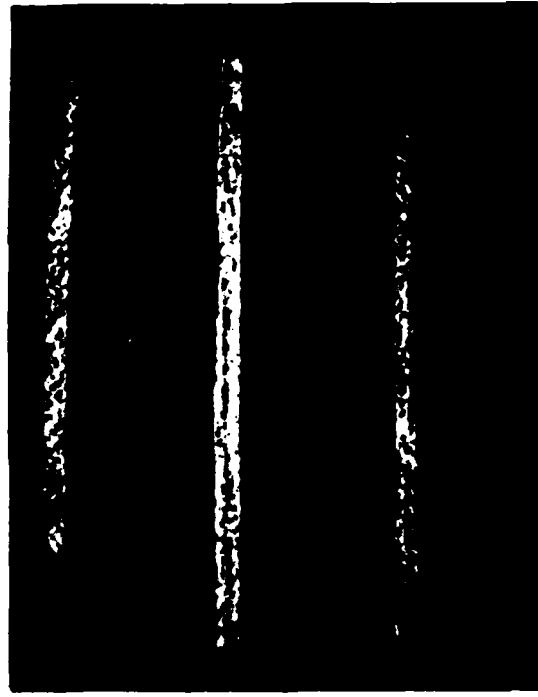
(a)

(b)

Fig. 33. (a) ROIR tomograms of the third plate weldment obtained from the U. S. Air Force, Kelly Supply Depot, reconstructed with the same scan parameters as in Fig. 31. (b) The corresponding radiograph.

66

4.6 Empirical Simulation of On-line Weld Evaluation

Finally, an experiment was performed to study the applicability of tomographic techniques for on-line, quasi-real time inspection in automated welding processes.

Two sections of the five inch diameter rocket motor casing were initially spot welded to hold the sections together. The unwelded joint was comprehensively scanned in the same manner as the Hercules welds. The location and orientation of the object were precisely marked. The joint was then welded using a standard Tungsten Inert Gas (TIG) welding process. The weldment was made to include an unwelded region, lack of fusion, single weld pass on the outer surface, and double weld passes, one on the outer surface and one on the inner surface. Several regions of the weld were intentionally made uneven. After the welding of the joint, the weldment was rescanned in the same configuration as before, using the same tomographic parameters. Geometric precision in object positioning was insured by an appropriate mounting mechanism.

The tomograms of the weldment cross section were reconstructed on a 256 x 256 grid with the pixel dimensions of 0.53 mm x 0.53 mm. The tomogram of the cross section prior to the welding is shown in Fig. 34, and the one obtained after the completion of welding is shown in Fig. 35. Visually, these tomograms do not display any difference. The difference image, shown in Fig. 36, obtained by subtracting the first tomogram from the second, displays clearly how the mass distributions in the two cases differ. We note that the TIG welding process does not add extra mass in the weldment region; it simply redistributes the mass.

The regions of different weld characteristics are marked in Fig. 36. Region T_1 is a single weld on the outer surface, region T_2 is a double
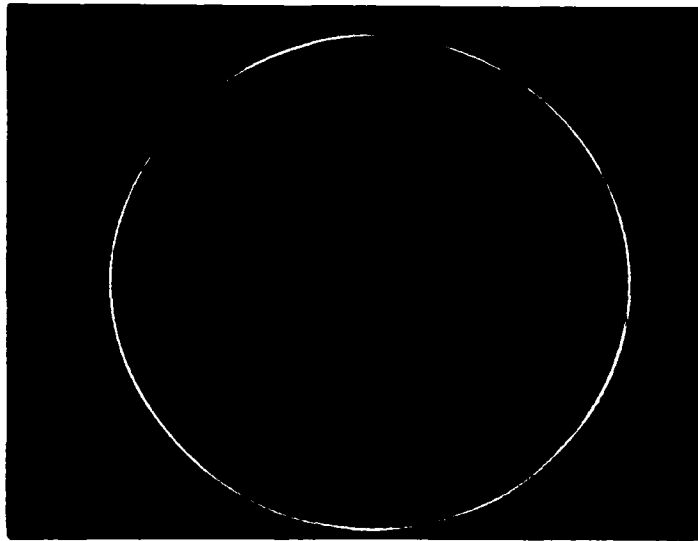
Fig. 34. Tomogram of the five-inch casing prior to the welding pass.
Source: Ir-192. Grid: 256 x 256. Pixel dimensions:
0.53 mm x 0.53 mm.
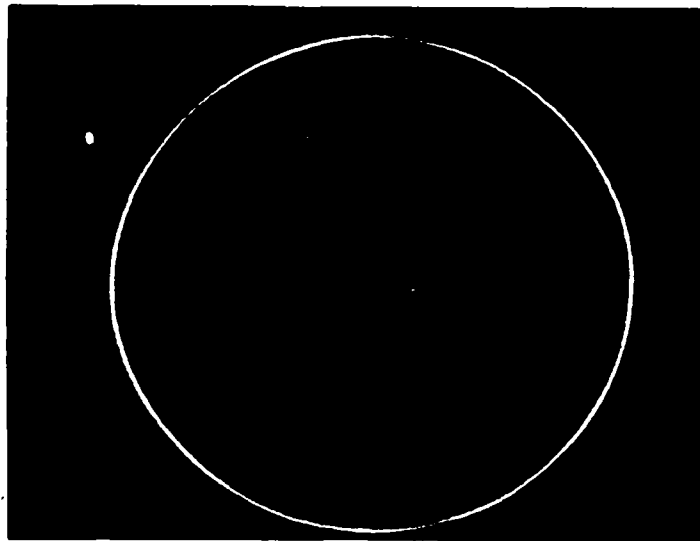
Fig. 35. Tomogram of the five-inch casing through the same plane
as in Fig. 34, after the completion of the welding pass.

weld, i.e., one weld on the outer surface and one on the inner surface, with parts of the inner weld uneven. Sections A_1 and A_2 in the region T_1 are regions of lack of fusion or missed joints. The point marked S in the region T_2 is the location of a bead formed on the inner surface during the spot welding. Region R_3 corresponds to the unwelded region.

The difference image displays a dark-bright band structure in the region of the object cross section. The circular pattern visible elsewhere is the circular artifact pattern, typical in tomographic images generated with a rotate-only geometry. These artifacts can be substantially suppressed by appropriate data smoothing and normalization

procedures. In the present analysis, only a simple data smoothing procedure was employed. The band structure in the difference image can arise for different reasons.

One possibility is that the object location and/or orientation with respect to the tomographic setup may shift between the consecutive scans. As an example of the effects introduced by object shifting, the tomogram in Fig. 35 was shifted by one pixel extent, 0.53 mm, along the positive x-axis, before obtaining the difference image. The corresponding difference image is shown in Fig. 37. We note that, owing to the circular symmetry of the object, a position shift can introduce only two diametrically opposite crossover points in the band structure. These are clearly seen at the top and bottom of the difference image in Fig. 37.

Since the band structure in Fig. 36 displays more than two crossover points, it cannot be attributed entirely to a shift in the object position. In particular, if the difference image in Fig. 36 is displayed on the same scale as that in Fig. 37, the shift effect can be assessed more
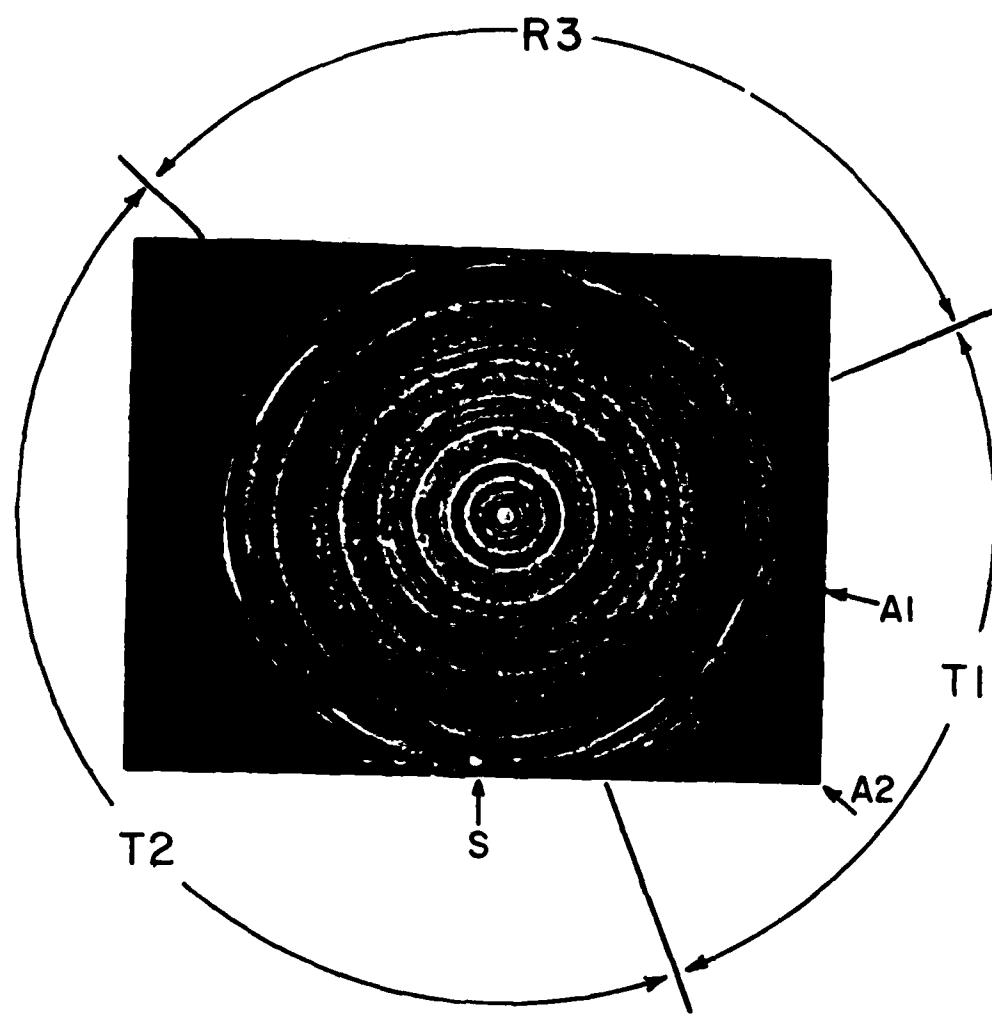
Fig. 36. The difference image obtained by subtracting the tomogram in Fig. 34 from that of Fig. 35. A_1 and A_2 correspond to regions containing lack of fusion or missed joints. The circular pattern visible in the tomogram is an artifact pattern.
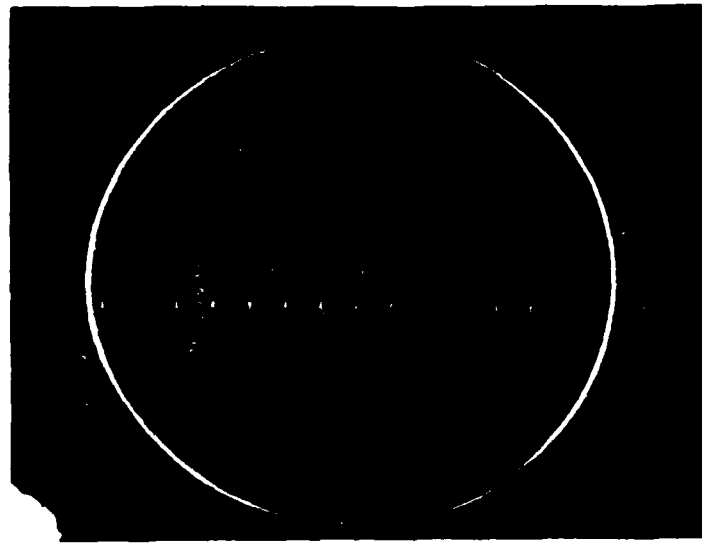
Fig. 37. An illustration of the band structure generated
entirely by a shift in the location of the object.
The image was obtained by shifting the weldment tomo-
gram (Fig. 35) by one pixel length along the x-axis
before subtracting the tomogram of Fig. 34.

realistically. Such a display is shown in Fig. 38, and a comparison with Fig. 37 indicates that the object location has been maintained very accurately. The mass density across the band structure in Fig. 37 varies from -4.7 to +4.8 (arbitrary units), whereas in Fig. 38 the range is -1.1 to 0.9. This indicates that, if at all, the position shift is a small fraction of one pixel size.

Another possibility leading to band structures is distortion of the object shape, caused by the heating during a welding process. This appears to be one of the factors contributing to the band structure in the present case. The redistribution of the mass due to welding, such as the typical formation of a crown along the weldment, changes the cross-sectional shape, and contributes to the band structure. Overall, visual inspection of the image in Fig. 36 indicates the presence of shape distortion. The regions Al and A2, locations of lack of fusion, are well demarked. The uneven nature of the weld, around the 7 o'clock region, is distinguishable; however, a portion of this is masked by circular artifacts crossing over the object region.

As noted earlier the circular artifacts can be reduced substantially. The use of the differencing method, however, is to detect the presence of defects. In most welding procedures, such as vacuum electron beam welding, a defective sample is simply rewelded rather than discarded. If, however, more detailed information is needed on a defective region, the tomographic data can be readily used for a rapid ROIR of that region. Reconstruction of a tomogram, or of any particular region of interest, can be accomplished within a few minutes. Due to the digital matrix form of the tomographic data, various manipulations of the data can be rapidly implemented via computer algorithms.

Fig. 38. The difference image of Fig. 36, displayed
on the same scale as in Fig. 37.

The results of the present prototype experiment indicate that tomo-graphic methods are applicable to on-line quasi-real time inspection of automated welding processes. In these processes, such as EB welding, the use of CT methods would eliminate the necessity of repressurizing the welding chamber to remove and inspect the object. The decisions regarding rewelding of the defective regions, and the rewelding procedure, can be accomplished in a matter of minutes, as opposed to a few hours needed

through the routine inspection methods. In addition, the tomographic data contains information on the shape. It is possible to assess the degree of distortion in cases where maintaining the object shape is crucial.

5. Summary and Conclusions

The program of research, the results, and pertinent conclusions regarding the applicability of CT methods for nondestructive inspection of weldments are summarized in this section. An evaluation of the applicability of these methods as on-line, quasi real time inspection techniques, in automated welding processes, is also included.

The research conducted under the present program involved tomographic examination of weldments of various types, contained in objects of differing characteristics. Since the detection and identification of various weldment defects depend crucially on the selection of tomographic parameters, emphasis was placed on studying the parametric dependence of spatial resolution. In addition, a study was conducted to examine the use of partial view tomography for imaging extended systems.

A laboratory prototype experiment was included in the research program to demonstrate the applicability of Computerized Tomography as an on-line, quasi real time inspection method in automated manufacturing processes.

The research was performed using the SMS EM-1 laboratory high-energy tomograph. The weldment types included the vacuum electron beam (EB) welds and the inert gas arc (heliarc) welds. There were three different types of objects bearing these weldments. One set of objects was composed of thin cylindrical #1042 steel shells, of the types used in the fabrication of certain tactical missile rocket motor casings. The second type was composed of cast aluminum components, welded together at several places. This object was a component of the space shuttle booster assembly. The last set of objects was composed of thin special alloy aluminum plates, which were sections of aircraft body panels. These objects were obtained from private

75

and government agencies involved in the aerospace industry related efforts.

The EB weldments of the rocket motor casings included by design a variety of defects, such as lack of fusion, cracks, voids, porosity, mis-joints, drop-through and undercuts. The aluminum casting and the aluminum test plates were objects rejected at the manufacturing end through different nondestructive inspection techniques. The EB weldments and the heliarc plate weldments were accompanied by radiographs. The cast aluminum object weldments were rejected on the basis of dye penetrant and visual inspection.

All of the weldments were comprehensively scanned with the SMS EM-1 Industrial Tomograph. The projection data obtained were used for recon-structing the cross-sectional images (tomograms). The information contained in tomograms was evaluated for detection, identification and assessment of various defects. Tomographic evaluations were compared with the available radiographic evaluations, to examine the relative merits of these tech-niques. From the results of the comparative study, information was obtained on necessary criteria for obtaining higher resolutions in CT examinations of weldments.

A comprehensive summary of detection of weldment flaws via various inspection methods is given in Table 2.

TABLE 2

Summary of Weldment Defects Evaluation

Defect/Feature	Method	Results and Comments
1. Lack of fusion/ Missed joints	1. Radiography	1. Completely unwelded regions are well resolved.
		2. In the case of partial fusion, some ambiguity existed in interpretation.
		3. Method relies on relative contrast, which leads to subjective evaluation at times.
		4. No cross-sectional information was obtained.
	2. Dye Penetration	1. Lack of fusion regions are detected, but no information is obtained about the sub-surface structure.
	3. CT	1. Resolution of completely unwelded regions is obtained on the basis of cross-sectional thickness assessments.
		2. Partial fusing is clearly detected from the shape of the cross section.
		3. Differencing techniques are available for improved resolution.
		4. All evaluations can be made quantitatively and rapidly.

77

TABLE 2 continued

Defect/Feature	Method	Results and Comments
2. Voids/Gaps	1. Radiography	1. Gaps are clearly resolved. In some cases, surface pittings are indistinguishable for clear gaps, due to the reliance of the method on contrast evaluation.
		2. Relative location of the voids is not possible, although their presence is detected.
	2. CT	1. Gaps are clearly resolved.
		2. Surface pittings are clearly distinguished since the cross-sectional data is obtained.
		3. Resolution of the voids or gaps diminishes (visually), for the feature extents smaller than the sampling extents.
		4. Quantitative methods are available to measure feature extents, as well as their relative locations.
3. Porosity	1. Radiography	1. Regions of porosity are well imaged, but in some cases ambiguity exists in interpretation.
		2. Relative location of the pores is not detectable.
		3. Very fine pores are detected.

78

TABLE 2 concluded

Defect/Feature	Method	Results and Comments
3. Porosity (contd)	2. CT	1. In general, porous areas have not been resolved, due to the sampling size. Finer collimation and lower photon energies are required for the resolution of pores in thin objects.
4. Undercuts	1. Radiography	1. Undercuts are distinguished, however, contrast interpretation is somewhat subjective.
	2. CT	1. Undercuts are unresolved due to the lack of fine collimation in the vertical direction.
5. Drop-through	1. Radiography	1. Drop-through areas are distinguished on the image, but their location is not possible to evaluate.
	2. CT	1. Drop-through areas are distinguished from the variations in the cross-sectional thickness and their location is evaluated.

79

The experimental study performed to evaluate the applicability of CT techniques for an on-line inspection of automated welding processes provided encouraging results. The experiment involved CT examinations of an object plane, prior to and after a TIG weld was performed. A quick evaluation of the weldment was obtained by analyzing the differences in mass distributions in the two situations. This difference imaging technique allowed detection of the unwelded regions, such as missed joints and lack of fusion. In addition, the technique permits an assessment of the object shape distortion. Use of such a technique, with finer collimation, would permit not only detection but also quantitative measurements of various defects.

The results obtained from this experimental study strongly indicate the feasibility of applying CT methods to automated welding processes such as vacuum electron beam welding of rocket motor casings. As shown in Fig. 39, a tomograph can be installed in the weld chamber itself and the weldment seams could be scanned, both prior to and after welding passes. An advantage in such an application is that the translational and rotational motions of the object are automatically provided by the positioning mechanism contained in the weld chamber. Since the EB welding process requires an accurate positioning of the seam, the positioning requirements for CT scans are readily fulfilled.

Objects such as rocket motor casings, typically receives these EB weld passes. These are called penetration passes, fusion pass and smoothing pass. The first pass penetrates the seam to the inner surface and fuses the joint ends together. The second pass is the main fusion pass and the final pass,

80
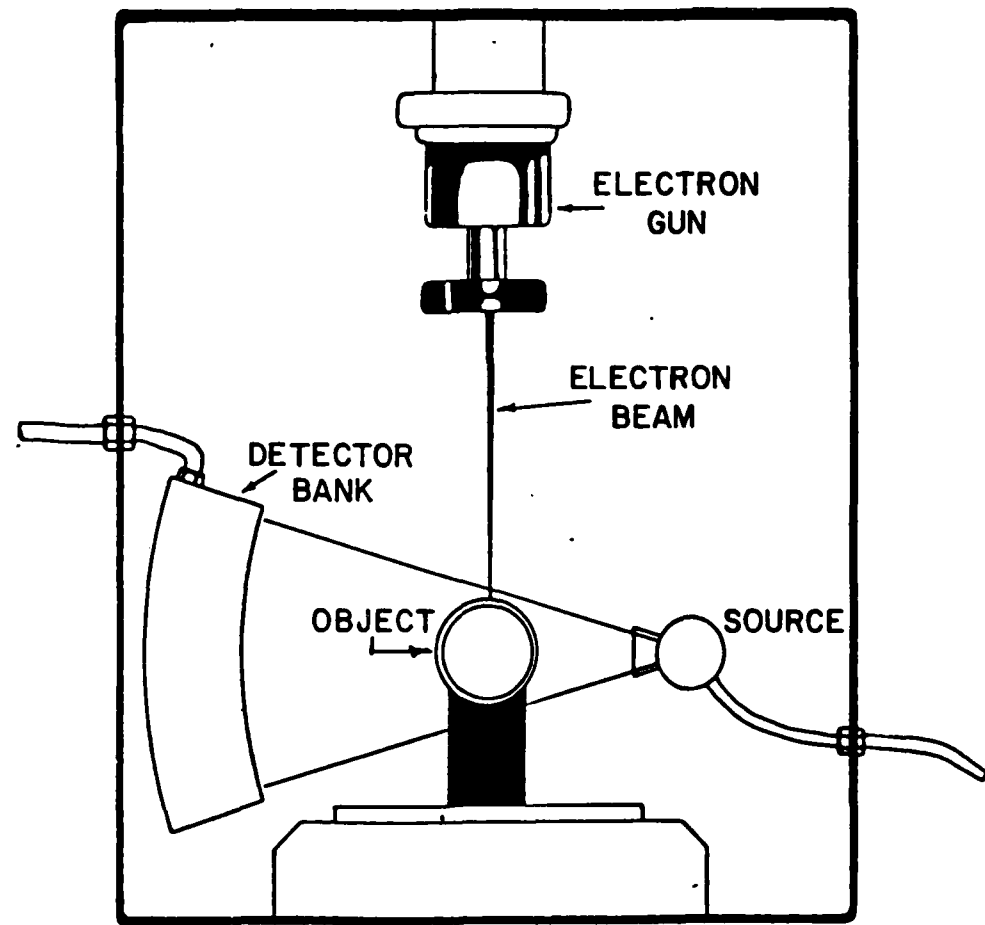
Figure 39. Design of a tomograph for on-line inspection in Electron Beam welding processes.

with a slightly defocused electron beam, smooths the weldment crown. The duration of each pass is approximately 15 to 20 seconds.

CT examinations can be readily performed between successive weld passes and corresponding tomograms can be rapidly reconstructed. The use of differencing techniques has the obvious advantage in that the anomalous areas can be quickly detected and reweldment of defective regions can be implemented without any undue loss of time. On-line inspection provided by this method eliminates the necessity of remounting the object, and has the added advantage of precisely matching the reweld location. Also, in those cases where a detailed examination of a feature is desired, an ROIR tomogram can be readily obtained and analyzed in detail.

The design of a tomograph, for such a specific application, would include a medium energy isotopic gamma ray source or an x-ray source, properly shielded for radiation. The detector bank design would include provisions for small detector apertures of 1 mm x 1 mm or smaller. The collimator design would also minimize scattering effects. The object motion and positioning is completely provided by the welding apparatus itself. The tomograph, therefore, is a static device and has the flexibility of locating it anywhere in the EB welding chamber. Effectively, the design is of a third generation "rotate only" type tomograph, ideally suited for the inspection of automated EB welding of rocket motor casings.

Currently, Scientific Measurement Systems, Inc. is conducting an extensive research program, supported in part by the National Science Foundation, to investigate the degree of spatial resolution attainable in industrial tomography. The program includes, among other topics, detailed research on various detection devices, the use of light piping, analytic and empirical

82

methods for differentiating the system response functions, and pattern recognition methods. It is anticipated that the results obtained under this research program will permit resolution of features 100 to 150 microns in extent. In view of this, it is strongly felt that CT techniques can be successfully applied to automated EB welding processes, as on-line quasi real time inspection methods.

Assessment of the cost-to-benefit ratios and projections on ultimate utilization volume are difficult to make. A telephone survey of the rocket motor casing manufacturers was made to assess the type of defects encountered in EB welding processes, the frequency of their occurance, inspection methods used and their relative success. Due to the proprietary nature of the information sought, it had been difficult to acquire sufficient information to accurately project the demand for CT inspection methods. The survey results, however, indicate that missed joint and lack of fusion types of defects have been difficult ones to detect via radiographic techniques. One source indicated that hydropressurizing techniques were used to detect and locate missed joint regions which were not detected by radiography. Of the total footage welded using automated EB welding processes, the survey indicated that approximately 3 to 6 percent were defective and needed reweldment. Although the amount and the nature of the information obtained from this survey is limited, it indicates that certain difficult inspection problems exist, which could be remedied by the use of CT techniques.

In final conclusion, the present study indicates that CT methods are applicable for nondestructive examination and evaluation of various types of weldments. The digital form of tomographic data offers advantages of quantitative measurements and rapid analysis via computer algorithms. The range and

83

the flexibility of the tomographic parameters indicate the possibility of achieving higher spatial resolution. Particularly, in view of the concurrent research, attainment of high spatial resolution in weldment examinations appears feasible.

Although limited information is obtained from a partial view tomography, the results have indicated that CT processes can provide a reasonable inspection of extended objects. If available, a priori information regarding the object system, along with suitable reconstruction algorithms, is used, the limited view tomography can be a valuable inspection method for extended systems. The results have also indicated that the CT methods can be successfully employed for on-line quasi real time inspection of automated welding processes.

6. References

1. W. A. Ellingson and H. Berger. "Three Dimensional Radiographic Imaging," in Research Techniques in Nondestructive Testing, Vol. 4, Ed. R. S. Sharpe, Academic Press, London (1980) pp. 1-38.

2. R. D. Evans. The Atomic Nucleus, McGraw-Hill Book Co., Inc. New York (1955).

3. A. P. Arya. Fundamentals of Nuclear Physics, Allyn and Bacon, Inc., Boston, Mass. (1966).

END

FILMED

5-83

DTIC